Cohesive GTN model for ductile fracture simulation

Noé Brice Nkoumbou Kaptchouang, Yann Monerie, Pierre-Guy Vincent, Frédéric Perales

Cohesive GTN model for ductile fracture simulation

Noé Brice Nkoumbou Kaptchouang[a,b], Yann Monerie[b,c,*], Pierre-Guy Vincent[a,b], Frédéric Perales[a,b]

[a] *Institut de Radioprotection et de Sûreté Nucléaire, B.P. 3, 13115 Saint-Paul-lez-Durance Cedex, France*
[b] *MIST Laboratory, IRSN-CNRS-UM, B.P. 3, 13115 Saint-Paul-lez-Durance Cedex, France*
[c] *LMGC, Univ Montpellier, CNRS, Montpellier, France*

Abstract

The present work addresses the micromechanical modeling and the simulation of crack initiation and propagation in ductile materials failing by void nucleation, growth and coalescence. A cohesive-volumetric approach is used and the overall material behavior is characterized both by a hardening bulk constitutive law and a softening surface traction-separation law embedded between each mesh of a finite element discretization. The traction-separation law sums up accross a surface all the ductile damage processes occurring in a narrow strain localization band, while the bulk behavior concerns the other elasto-plastic effects. The proposed cohesive zone model is based on a micromechanical approach where the Gurson-Tvergaard-Needleman ductile damage model is adapted to the reduced kinematics of a surface while ensuring the complete effect of the strain rate or stress triaxiality both on the local plasticity and on the void growth. The corresponding cohesive model is implemented in the XPER computer code using the Non-Smooth Contact Dynamics method where cohesive models are introduced as mixed boundary conditions between each volumetric finite element. The present approach is applied to the simulation of crack growth in a standard ferritic steel. Results are compared with available experimental data. The efficiency of the proposed cohesive-GTN model is underlined since the shape of the cohesive law and its mechanical parameters arise directly from the micromechanical approach without any *ad hoc* fitting parameter.

Keywords: Ductile fracture, Cohesive zone model, GTN model, Crack growth simulation, Triaxiality effects

1

*Corresponding author
Email address: yann.monerie@umontpellier.fr (Yann Monerie)

Nomenclature

Ω, $\partial\Omega$	domain and its boundary
$\dot{\boldsymbol{E}}$	strain rate
$\dot{E}_{\mathsf{m}}$, $\dot{E}_{\mathsf{eq}}$	hydrostatic and equivalent parts of the strain rate
$\eta_{\dot{\boldsymbol{E}}}$	strain rate triaxiality, equation (4)
$\dot{p}$	in-plane strain rate
f	porosity
f^*	effective porosity related to the void coalescence, equation (8)
f_c	porosity at onset of void coalescence
f_f	porosity at final failure
σ_0	yield stress of the matrix material surrounding the voids
σ_y	flow strength of the matrix material
$\bar{\varepsilon}$	average plastic strain of the matrix material
$\boldsymbol{R}$, $[\boldsymbol{u}]$	stress vector and displacement jump across the cohesive zone
$\boldsymbol{n}$, $\boldsymbol{t}$, $\boldsymbol{s}$	vectors defining the normal-tangent basis
h	thickness of the localization band summarized by the cohesive zone
H, D	functions of Gurson model, equation (2)
χ	couple of variables $\{\eta_{\dot{\boldsymbol{E}}}, q_1 f^*(f)\}$

1. Introduction

Many materials used in nuclear plants are polycristalline materials that exhibit a ductile behavior at high temperature, e.g. ceramic materials such as uranium dioxide [1] or mixed oxide fuels, metallic alloys used for the reactor pressure vessels [2], structural components within the vessels, etc. Simulation of the fracture of these materials under accident conditions is of great interest when assessing the safety of nuclear plants. One of the process of ductile fracture is the nucleation and growth of microscopic voids under accumulation of plastic strain in some regions [3, 4]. As a consequence, these regions are softened and the deformations can localize into some narrow band, referred as *fracture process zone*, where coalescence of voids occurs and leads to main cracks [5].

On one hand, a widely used framework to describe such a damage process in ductile materials is the continuum micromechanics, based on a physical modeling of the kinematics of voids nucleation, growth and coalescence inside a matrix material. Within this approach, the Gurson-Tvergaard-Needleman (GTN) model [6–9] is surely the most widespread model to characterize the ductile fracture.

On the other hand, Cohesive Zone Models (CZM) are widely used as numerical models leading to creation of surface as a limit case of strain localization, [10, 11] among others. This phenomenological approach of fracture is based on the pioneering works of [12] and [13] who proposed to introduce a process zone at the crack tip in order to avoid the unrealistic unbounded stresses predicted by Linear Elastic Fracture Mechanics. In such an approach, the stress remains finite and tends to vanish while the crack tip is opening. In the standard cohesive surface theory of fracture, the crack growth is modeled as a decohesion of two surfaces within a continuum material. Therefore, the cohesive stress corresponds to the amount of stress which is needed to initiate the separation of the two surfaces. In this framework, the overall material behavior is characterized by two constitutive relations, the volumetric (bulk) stress–strain constitutive law and the traction–separation law across the cohesive surface embedded in a three-dimensional continuum. The traction–separation law is expressed as a relationship $\boldsymbol{R} = \mathcal{R}([\boldsymbol{u}])$ between the stress vector $\boldsymbol{R}$ and the displacement jump $[\boldsymbol{u}]$ across the two surfaces. For a given material, the shape of the curve $\mathcal{R}([\boldsymbol{u}])$ is generally unknown and many *a priori* shape functions are proposed in the literature, see [14–17] to cite few. The CZM is thus fully determined by the data of some mechanical surface parameters as cohesive energy and toughness [16, 18, 19].

It is worth noting that the particular case of the simulation of tearing of ductile metal plates with the help of

cohesive zone models has recently given rise to several papers [20–23]. As pointed out by [23], cohesive zone modeling is often combined in practical situations with shell modeling. Cohesive zone models have been elaborated and calibrated in these works, using numerical simulations and sometimes experimental results. In [21], a plate tearing problem is simulated and the measured overall force–displacement response is used to calibrate the cohesive zone. In [20], the complex sequence of events that occurs during failure is studied in details with a GTN model. During a mode I loading crack growth, the fracture process is simulated by a 2D plane strain finite element model. Then, the traction–separation relationship of the cohesive zone is determined. This work was extended in [23] by expanding the model to 3D.

The parameters of any CZM corresponding to a bulk ductile damage model don't have to be considered as pure material parameters since the ductile failure based on void initiation, growth and coalescence is strongly dependent on the local stress and strain states [9, 24, 25]. Previous works have introduced *ad hoc* dependence of cohesive parameters on surrounding plastic state. For example, [26, 27] propose to add a dependence on the accumulated plastic strain of the material adjacent to the cohesive zone. In [28, 29], a stress triaxiality dependent cohesive model is formulated by the use of elastic-plastic constitutive relations combined with a softening law under plane strain and plane stress conditions. The behavior of the traction separation law up to the peak stress is established to replicate the linear elastic and strain hardening behavior of an undamaged material in plane strain [30] and plane stress [29]. The resulting behavior is therefore a function of the path in the stress space (thus the stress triaxiality) and elastic-plastic constants. The softening after the peak stress is characterized by an exponential smoothing function. Another approach to determine the ductile cohesive parameters from a micromechanical basis consists in considering a Representative Volume Element (RVE) composed of a Gurson-like material and identifying the cohesive parameters of an *a priori* given CZM to fit the overall response of the RVE. This idea has been introduced by [16] who studied the behavior of a GTN unit cell under uniaxial strain conditions. Since the void growth and coalescence at high stress triaxiality is the main microscopic mechanism of ductile fracture, this approach has been extended by [30–32] to take into account the local stress triaxiality as an internal variable of a cohesive model. They have determined the cohesive parameters dependence on the stress triaxiality by the numerical study of a plane strain or axisymmetric unit cell under different biaxial stress loadings. This approach has been further developed by [33, 34] for the case of rate-dependent GTN-type model.

Following the idea that the traction–separation law should represent the failure behavior of a unit material cell, the present work proposes to derive a CZM for ductile materials from a micromechanical approach. The objective is to obtain a CZM whose the shape as well as the parameters directly derive from a bulk ductile damage model, namely here the GTN model. The present paper is organized as follows. The second section details the modeling and the derivation of the CZM. The third section is devoted to its numerical implementation in the XPER computer code. In a fourth section, the simulation of crack growth in a standard ferritic steel shows the relevance of the approach by comparison to available experimental data.

2. Cohesive zone model for ductile failure

2.1. GTN model

Let us recall that Gurson yield surface [6] is based on the analysis of a hollow sphere (domain Ω, porosity f) made of a homogeneous and incompressible plastic matrix obeying to a von Mises yield criterion (J2 plasticity, yield stress σ_0) and subjected to a homogeneous macroscopic strain rate $\dot{\boldsymbol{E}}$ on its outer boundary $\partial\Omega$, $\boldsymbol{v} = \dot{\boldsymbol{E}} \cdot \boldsymbol{x}$ on $\partial\Omega$, where $\boldsymbol{v}$ is the velocity field and $\boldsymbol{x}$ is the position vector. The effective dissipation potential corresponding to Gurson yield surface reads [6, 35]:

$$\Phi^G(\dot{\boldsymbol{E}}) = \sigma_0 \int_f^1 \sqrt{\frac{4(\dot{E}_{\mathsf{m}})^2}{y^2} + (\dot{E}_{\mathsf{eq}})^2}\, dy \tag{1}$$

where $\dot{E}_{\mathsf{m}}$ and $\dot{E}_{\mathsf{eq}}$ are respectively the hydrostatic and equivalent strain rates, $\dot{E}_{\mathsf{m}} = (1/3)\,\mathrm{tr}\,\dot{\boldsymbol{E}}$, $\dot{E}_{\mathsf{eq}} = \sqrt{(2/3)\dot{\boldsymbol{E}}^{\mathsf{d}} : \dot{\boldsymbol{E}}^{\mathsf{d}}}$, $\dot{\boldsymbol{E}}^{\mathsf{d}} = \dot{\boldsymbol{E}} - \dot{E}_{\mathsf{m}}\,\boldsymbol{i}$ denotes the deviatoric part of the effective strain rate, and $\boldsymbol{i}$ is the second-

order identity tensor. A general expression of the integral (1) can be found in [35]:

$$\Phi^G(\dot{\boldsymbol{E}}) = \sigma_0 \dot{E}_{\mathsf{eq}} \left[3\eta_{\dot{\boldsymbol{E}}} H(\eta_{\dot{\boldsymbol{E}}}, f) + D(\eta_{\dot{\boldsymbol{E}}}, f)\right] \tag{2}$$

with

$$H(\eta_{\dot{\boldsymbol{E}}}, f) = \frac{2}{3}\left(\operatorname{arcsinh}\left(\frac{2\eta_{\dot{\boldsymbol{E}}}}{f}\right) - \operatorname{arcsinh}\left(2\eta_{\dot{\boldsymbol{E}}}\right)\right) \quad \text{and} \quad D(\eta_{\dot{\boldsymbol{E}}}, f) = \sqrt{(2\eta_{\dot{\boldsymbol{E}}})^2 + 1} - \sqrt{(2\eta_{\dot{\boldsymbol{E}}})^2 + f^2} \tag{3}$$

where the effective strain rate triaxiality reads

$$\eta_{\dot{\boldsymbol{E}}} = \frac{\dot{E}_{\mathsf{m}}}{\dot{E}_{\mathsf{eq}}} \tag{4}$$

The macroscopic stress $\boldsymbol{\Sigma} = \partial\Phi^G/\partial\dot{\boldsymbol{E}}$ is derived from the effective potential (2)

$$\Sigma_{\mathsf{m}} = \sigma_0 H(\eta_{\dot{\boldsymbol{E}}}, f) \quad \text{and} \quad \Sigma_{\mathsf{eq}} = \sigma_0 D(\eta_{\dot{\boldsymbol{E}}}, f) \tag{5}$$

where $\Sigma_{\mathsf{m}} = (1/3)\operatorname{tr}\boldsymbol{\Sigma}$ is the hydrostatic stress, $\Sigma_{\mathsf{eq}} = \sqrt{(3/2)\boldsymbol{\Sigma}^{\mathsf{d}} : \boldsymbol{\Sigma}^{\mathsf{d}}}$ the equivalent stress and $\boldsymbol{\Sigma}^{\mathsf{d}} = \boldsymbol{\Sigma} - \Sigma_{\mathsf{m}}\boldsymbol{i}$ the deviatoric part of $\boldsymbol{\Sigma}$. Gurson yield criterion is thus obtained by eliminating the kinematic parameter $\eta_{\dot{\boldsymbol{E}}}$ between the hydrostatic and equivalent stresses in (5):

$$\phi^{\mathsf{G}}(\boldsymbol{\Sigma}, f) = \frac{\Sigma_{\mathsf{eq}}^2}{\sigma_0^2} + 2f\cosh\left(\frac{3}{2}\frac{\Sigma_{\mathsf{m}}}{\sigma_0}\right) - 1 - f^2 = 0 \tag{6}$$

Various modifications of the Gurson criterion have been progressively introduced in the literature to better fit unit-cell simulations or to take into account cavities interaction and coalescence, etc and can be summarized by the so-called Gurson-Tvergaard-Needleman (GTN) model [8]:

$$\phi^{\mathsf{GTN}}(\boldsymbol{\Sigma}, f) = \frac{\Sigma_{\mathsf{eq}}^2}{\sigma_0^2} + 2q_1 f^*\cosh\left(\frac{3}{2}q_2\frac{\Sigma_{\mathsf{m}}}{\sigma_0}\right) - 1 - q_3 f^{*2} = 0 \tag{7}$$

where $q_1, q_2, q_3 = q_1^2$ are constants and f^* is an effective porosity related to the void coalescence:

$$f^* = \begin{cases} f & \text{for } \ 0 \le f \le f_c \\ f_c + \dfrac{f_u^* - f_c}{f_f - f_c}(f - f_c) & \text{for } f_c \le f \end{cases} \tag{8}$$

where f_c is the porosity at onset of void coalescence, f_f is the fracture porosity, $f^*(f_f) = f_u^* = 1/q_1$. The following notation is introduced $k = (f_u^* - f_c)/(f_f - f_c)$. Isotropic hardening can be introduced by replacing σ_0 with $\sigma_y(\bar{\varepsilon})$ in equation (7), where σ_y is the flow strength of the material surrounding the void. The scalar variable $\bar{\varepsilon}$ is interpreted as an 'average' plastic strain of the matrix material surrounding the void. Its evolution is governed by an equivalent plastic work expression:

$$\boldsymbol{\Sigma} : \dot{\boldsymbol{E}} = (1 - f)\sigma_y\dot{\bar{\varepsilon}} \tag{9}$$

The evolution of the void volume fraction is given by

$$\dot{f} = \dot{f}_g + \dot{f}_n \tag{10}$$

where $\dot{f}_g$ is the void growth rate, derived from the conservation of mass

$$\dot{f}_g = (1 - f)\operatorname{tr}\dot{\boldsymbol{E}} \tag{11}$$

and where $\dot{f}_n$ is the rate of void nucleation. In case of strain controlled nucleation, [36] suggest to approximate the nucleation of new cavities by a normal distribution

$$\dot{f}_n = A\dot{\bar{\varepsilon}} \quad \text{where} \quad A(\bar{\varepsilon}) = \frac{f_N}{s_N\sqrt{2\pi}}\exp\left(-\frac{1}{2}\left(\frac{\bar{\varepsilon} - \epsilon_N}{s_N}\right)^2\right) \tag{12}$$

where f_N is the volume fraction of void nucleating particles, ϵ_N is an average nucleation strain parameter and s_N is a standard deviation. By doing so, the rate of void nucleation depends on the 'average' plastic strain $\bar{\varepsilon}$ and its time derivative.

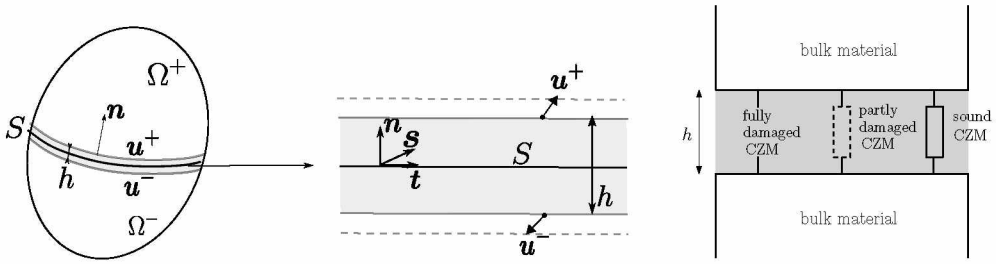

Figure 1: Displacement jump across a localization band of thickness h. The ductile damage process is summarized inside this band with the help of a surface cohesive zone model having the same behavior as a bulk GTN model. The damage intensity corresponds to the effective porosity given in (8).

2.2. Cohesive interface model

Let us consider that the material domain Ω is made of an elastic plastic material composed of two regions, Ω^- and Ω^+, separated by a strain localization band (unit normal vector $\boldsymbol{n}$), Figure 1. Outside the localization band, the material follows a J2 plasticity model without damage. Ductile damage occurs only inside the strain localization band and its behavior is described by the GTN model (7). The *thickness* h of the localization band is small compared to a characteristic length of Ω. This narrow band is then modeled as a cohesive surface S between Ω^- and Ω^+ as usually done in problems of adhesive solids [37, 38]. Designating by $\boldsymbol{u}^+$ and $\boldsymbol{u}^-$ the respective values of the displacement fields at the boundaries of Ω^+ and Ω^- shared with S, the displacement jump across S is defined as:

$$[\boldsymbol{u}] = \boldsymbol{u}^+ - \boldsymbol{u}^- = [u_{\mathsf{n}}]\boldsymbol{n} + [u_{\mathsf{t}}]\boldsymbol{t} + [u_{\mathsf{s}}]\boldsymbol{s} \tag{13}$$

in the local basis ($\boldsymbol{n}$, $\boldsymbol{t}$, $\boldsymbol{s}$) where $\boldsymbol{t}$ and $\boldsymbol{s}$ are two unit vectors defining the tangent plane. Following [37, 39, 40], the strain rate on the cohesive surface can be approximated with the help of a scaling rule:

$$\dot{\boldsymbol{E}} \approx \frac{[\dot{\boldsymbol{u}}] \otimes_s \boldsymbol{n}}{h} = \frac{[\dot{u}_i]n_j + [\dot{u}_j]n_i}{2h} = \begin{bmatrix} \dfrac{[\dot{u}_{\mathsf{n}}]}{h} & \dfrac{[\dot{u}_{\mathsf{t}}]}{2h} & \dfrac{[\dot{u}_{\mathsf{s}}]}{2h} \\ \dfrac{[\dot{u}_{\mathsf{t}}]}{2h} & 0 & 0 \\ \dfrac{[\dot{u}_{\mathsf{s}}]}{2h} & 0 & 0 \end{bmatrix} \tag{14}$$

All these softening effects occurring into the localization band are here summarized into a zero thickness cohesive surface. In the present work, the parameter h is thus more related to the thickness of the localization band than to the void spacing length as previously proposed in [28, 31, 32, 41, 42].

In such an approximation, the in-plane components of the strain rate are neglected. The hydrostatic part and the equivalent part of the strain rate read respectively

$$\dot{E}_{\mathsf{m}} = \frac{1}{3}\frac{[\dot{u}_{\mathsf{n}}]}{h}, \quad \dot{E}_{\mathsf{eq}} = \frac{2}{3}\sqrt{\left(\frac{[\dot{u}_{\mathsf{n}}]}{h}\right)^2 + \frac{3}{4}\frac{[\dot{u}_{\mathsf{t}}]^2}{h^2} + \frac{3}{4}\frac{[\dot{u}_{\mathsf{s}}]^2}{h^2}}$$

The strain rate triaxiality is thus obtained as

$$\eta_{\dot{\boldsymbol{E}}} = \frac{[\dot{u}_{\mathsf{n}}]}{2\sqrt{[\dot{u}_{\mathsf{n}}]^2 + \frac{3}{4}[\dot{u}_{\mathsf{t}}]^2 + \frac{3}{4}[\dot{u}_{\mathsf{s}}]^2}}$$

The strain rate triaxiality $\eta_{\dot{\boldsymbol{E}}}$ is bounded by above by 1/2, limiting the void growth rate in equation (11). This is a strong limitation to develop surface cohesive model for ductile damage. This limitation is directly linked to the reduced kinematics of a surface. To overcome this limitation, two strategies can be considered. First, information about the current loading state can be transferred from the volumetric domains Ω^+ and

Ω^- to the cohesive zone S. The underlying hypothesis is that the loading state inside the cohesive band remains close to the nearest continuum elements adjacent to the cohesive band. This idea was introduced by [27], who proposed a cohesive law depending on the average of the accumulated plastic strain over a bulk finite element adjacent to the cohesive zone. This idea was further extended by [31] who introduced the cohesive parameters dependence on the stress triaxiality of a continuum element adjacent to the cohesive zone. In the latter, the evolution of cohesive parameters with respect to the stress triaxiality was identified by simulating the behavior of a plane strain element obeying to a GTN model under different biaxial loadings.

Second, the dependence of cohesive models on the stress–strain state can be improved by incorporating additional in-plane terms in the cohesive strain rate (14). [43] propose to determine these in-plane terms through the values at each side of the cohesive zone (so from the nearest volumetric elements) to enforce a continuity of the strain. In the present work, in order to enhance the range of stress and strain states affordable by the cohesive model, it is proposed to extend the cohesive kinematics by introducing an additional in-plane strain rate $\dot{p}$:

$$\dot{\boldsymbol{E}} \approx \frac{[\dot{\boldsymbol{u}}] \otimes_s \boldsymbol{n}}{h} + \dot{p}\,(\boldsymbol{t} \otimes_s \boldsymbol{t} + \boldsymbol{s} \otimes_s \boldsymbol{s}) = \begin{bmatrix} \dfrac{[\dot{u}_{\mathsf{n}}]}{h} & \dfrac{[\dot{u}_{\mathsf{t}}]}{2h} & \dfrac{[\dot{u}_{\mathsf{s}}]}{2h} \\ \dfrac{[\dot{u}_{\mathsf{t}}]}{2h} & \dot{p} & 0 \\ \dfrac{[\dot{u}_{\mathsf{s}}]}{2h} & 0 & \dot{p} \end{bmatrix} \tag{15}$$

This simple choice allows the strain-rate triaxiality $\eta_{\dot{\boldsymbol{E}}}$ to range within $]-\infty, +\infty[$. The rate $\dot{p}$ depends on the loading state provided by the volumetric finite element adjacent to the cohesive zone as presented in section 3.

2.3. Traction–separation law

Since the local behavior on S is described by the GTN plasticity model, the surface stress vector is related to the strain rate

$$\boldsymbol{R} = \boldsymbol{\Sigma} \cdot \boldsymbol{n} = \left(\Sigma_{\mathsf{m}} \boldsymbol{i} + \frac{2}{3} \frac{\Sigma_{\mathsf{eq}}}{\dot{E}_{\mathsf{eq}}} \dot{\boldsymbol{E}}^{\mathsf{d}} \right) \cdot \boldsymbol{n} \tag{16}$$

with Σ_{m} and Σ_{eq} given by (5). A normalized stress tensor $\bar{\boldsymbol{\Sigma}}$ is then defined and the stress vector $\boldsymbol{R}$, or cohesive stress, reads

$$\bar{\boldsymbol{\Sigma}} = \frac{1}{\sigma_y} \boldsymbol{\Sigma} \quad \text{thus} \quad \boldsymbol{R} = \sigma_y \, \bar{\boldsymbol{\Sigma}} \cdot \boldsymbol{n} \quad \text{where} \quad \bar{\boldsymbol{\Sigma}} \cdot \boldsymbol{n} = \begin{cases} \bar{\Sigma}_{\mathsf{nn}} = \dfrac{1}{q_2} H(\chi) + \dfrac{4}{9} D(\chi) \dfrac{1}{\dot{E}_{\mathsf{eq}}} \left(\dfrac{[\dot{u}_{\mathsf{n}}]}{h} - \dot{p} \right) \\ \bar{\Sigma}_{\mathsf{nt}} = \dfrac{1}{3} D(\chi) \dfrac{1}{\dot{E}_{\mathsf{eq}}} \dfrac{[\dot{u}_{\mathsf{t}}]}{h} \\ \bar{\Sigma}_{\mathsf{ns}} = \dfrac{1}{3} D(\chi) \dfrac{1}{\dot{E}_{\mathsf{eq}}} \dfrac{[\dot{u}_{\mathsf{s}}]}{h} \end{cases} \tag{17}$$

and

$$\dot{E}_{\mathsf{eq}} = \frac{2}{3} \sqrt{\left(\frac{[\dot{u}_{\mathsf{n}}]}{h} - \dot{p} \right)^2 + \frac{3}{4} \frac{[\dot{u}_{\mathsf{t}}]^2}{h^2} + \frac{3}{4} \frac{[\dot{u}_{\mathsf{s}}]^2}{h^2}}, \quad \eta_{\dot{\boldsymbol{E}}} = \frac{\dfrac{[\dot{u}_{\mathsf{n}}]}{h} + 2\dot{p}}{2\sqrt{\left(\dfrac{[\dot{u}_{\mathsf{n}}]}{h} - \dot{p} \right)^2 + \dfrac{3}{4} \dfrac{[\dot{u}_{\mathsf{t}}]^2}{h^2} + \dfrac{3}{4} \dfrac{[\dot{u}_{\mathsf{s}}]^2}{h^2}}} \tag{18}$$

where χ stands for the couple of variables $\chi = \{\eta_{\dot{\boldsymbol{E}}}, q_1 f^*(f)\}$. Equation (17) shows that this cohesive formulation can be used in 3D since the stress vector is fully described and under mixed mode conditions since all components of the displacement jump have an independent role. The effect of the strain-rate triaxiality is taken into account through the variable χ in functions H and D.

The effective porosity f^* is expressed in terms of porosity f with (8). The evolution law of porosity (10) (including nucleation) reads

$$\dot{f} = (1-f)\left(\frac{[\dot{u}_{\mathsf{n}}]}{h} + 2\dot{p}\right) + A\dot{\bar{\varepsilon}} \tag{19}$$

and hardening is estimated through the average plastic strain $\bar{\varepsilon}$ using (9)

$$\dot{\bar{\varepsilon}} = \frac{1}{1-f}\left(\bar{\Sigma}_{\mathsf{nn}}\frac{[\dot{u}_{\mathsf{n}}]}{h} + \bar{\Sigma}_{\mathsf{nt}}\frac{[\dot{u}_{\mathsf{t}}]}{h} + \bar{\Sigma}_{\mathsf{ns}}\frac{[\dot{u}_{\mathsf{s}}]}{h} + \left(\bar{\Sigma}_{\mathsf{tt}} + \bar{\Sigma}_{\mathsf{ss}}\right)\dot{p}\right) \tag{20}$$

$$\bar{\Sigma}_{\mathsf{tt}} = \bar{\Sigma}_{\mathsf{ss}} = \frac{1}{q_2}H(\chi) - \frac{2}{9}D(\chi)\frac{1}{\dot{E}_{\mathsf{eq}}}\left(\frac{[\dot{u}_{\mathsf{n}}]}{h} - \dot{p}\right) \tag{21}$$

It is worth noting that the evolution law of $\bar{\varepsilon}$ is independent of the hardening law $\sigma_y(\bar{\varepsilon})$. Moreover we underline that this GTN traction-separation law can simulate ductile fracture as soon as the porosity rate $\dot{f}$ is not vanishing. In other words, there is no need for macroscopic crack like defect to initiate and propagate a ductile crack with this model. We chose in the sequel to illustrate the ability of the model a compact tension specimen but other situations can be treated as for example notched tensile bars.

2.4. Time integration of the constitutive equations

For sake of simplicity, the dependence in time is omitted for the current time t, and thus $\boldsymbol{E}$, f and $\bar{\varepsilon}$ denote respectively the strain, the porosity and the average plastic strain at time t. Their values at the previous time step $t-\delta t$ are denoted by a superscript $(t-\delta t)$, $\boldsymbol{E}^{(t-\delta t)}$, $f^{(t-\delta t)}$ and $\bar{\varepsilon}^{(t-\delta t)}$. The strain increment $\delta\boldsymbol{E} = \boldsymbol{E} - \boldsymbol{E}^{(t-\delta t)}$ is introduced. Using an explicit scheme, the time discretized equations thus read

$$f = f^{(t-\delta t)} + (1-f^{(t-\delta t)})\,(\delta E_{\mathsf{nn}} + 2\,\delta p) + A(\bar{\varepsilon}^{(t-\delta t)})\,\delta\bar{\varepsilon} \tag{22}$$

$$\bar{\varepsilon} = \bar{\varepsilon}^{(t-\delta t)} + \delta\bar{\varepsilon} \quad \text{with} \quad \delta\bar{\varepsilon} = \frac{\bar{\Sigma}_{\mathsf{nn}}\,\delta E_{\mathsf{nn}} + 2\,\bar{\Sigma}_{\mathsf{nt}}\,\delta E_{\mathsf{nt}} + 2\,\bar{\Sigma}_{\mathsf{ns}}\,\delta E_{\mathsf{ns}} + \bar{\Sigma}_{\mathsf{tt}}\,\delta p + \bar{\Sigma}_{\mathsf{ss}}\,\delta p}{1-f^{(t-\delta t)}} \tag{23}$$

and

$$\begin{cases} \bar{\Sigma}_{\mathsf{nn}} = \dfrac{1}{q_2}H(\chi^{(t-\delta t)}) + \dfrac{4}{9}D(\chi^{(t-\delta t)})\dfrac{\delta E_{\mathsf{nn}} - \delta p}{(\delta\boldsymbol{E})_{\mathsf{eq}}} \\ \bar{\Sigma}_{\mathsf{nt}} = \dfrac{2}{3}D(\chi^{(t-\delta t)})\dfrac{\delta E_{\mathsf{nt}}}{(\delta\boldsymbol{E})_{\mathsf{eq}}} \\ \bar{\Sigma}_{\mathsf{ns}} = \dfrac{2}{3}D(\chi^{(t-\delta t)})\dfrac{\delta E_{\mathsf{ns}}}{(\delta\boldsymbol{E})_{\mathsf{eq}}} \\ \bar{\Sigma}_{\mathsf{tt}} = \bar{\Sigma}_{\mathsf{ss}} = \dfrac{1}{q_2}H(\chi^{(t-\delta t)}) - \dfrac{2}{9}D(\chi^{(t-\delta t)})\dfrac{\delta E_{\mathsf{nn}} - \delta p}{(\delta\boldsymbol{E})_{\mathsf{eq}}} \\ \eta_{\dot{\boldsymbol{E}}} = \dfrac{(\delta\boldsymbol{E})_{\mathsf{m}}}{(\delta\boldsymbol{E})_{\mathsf{eq}}} \end{cases} \tag{24}$$

where $\chi^{(t-\delta t)}$ stands now for $\{\eta_{\dot{\boldsymbol{E}}}, q_1 f^*(f^{(t-\delta t)})\}$. Thus, knowing the strain tensor at time t, together with the strain, porosity and average strain at time $t-\delta t$, the porosity and the average strain are updated using equations (22), (23) and (24). Then components of the cohesive stress are evaluated straightforwardly at time t

$$\begin{cases} R_{\mathsf{n}} = \sigma_y(\bar{\varepsilon})\left(\dfrac{1}{q_2}H(\chi) + \dfrac{4}{9}D(\chi)\dfrac{\delta E_{\mathsf{nn}} - \delta p}{(\delta\boldsymbol{E})_{\mathsf{eq}}}\right) \\ R_{\mathsf{t}} = \sigma_y(\bar{\varepsilon})\dfrac{2}{3}D(\chi)\dfrac{\delta E_{\mathsf{nt}}}{(\delta\boldsymbol{E})_{\mathsf{eq}}} \\ R_{\mathsf{s}} = \sigma_y(\bar{\varepsilon})\dfrac{2}{3}D(\chi)\dfrac{\delta E_{\mathsf{ns}}}{(\delta\boldsymbol{E})_{\mathsf{eq}}} \end{cases} \tag{25}$$

2.5. Traction–separation behavior under various loadings

In order to illustrate the potentialities of the corresponding GTN traction–separation law, we use a Swift-like model to describe the hardening of the material

$$\sigma_y(\bar{\varepsilon}) = \sigma_0(1 + K\bar{\varepsilon})^{1/n} \tag{26}$$

where the yield stress σ_0 and the constants K and n are set to fit the experimental plastic flow data given by [32]. The material parameters of the study are specified in Table 1, where Y denotes the Young modulus and ν the Poisson ratio.

Elasticity	Y	ν						
	210 GPa	0.3						
Hardening	σ_0	K	n					
	470 MPa	35.0	4.5					
GTN	q_1	q_2	f_0	k	f_c	f_N	ϵ_N	s_N
	1.5	1.0	0.0025	3.4	0.021	0.02	0.3	0.1

Table 1: Material parameters for a ferritic steel StE460 (German designation) from [32].

First, let us consider a constant axisymmetric strain rate with the following strain

$$\boldsymbol{E} = \begin{bmatrix} \dot{E}_{\mathsf{nn}} & 0 & 0 \\ 0 & r\,\dot{E}_{\mathsf{nn}} & 0 \\ 0 & 0 & r\,\dot{E}_{\mathsf{nn}} \end{bmatrix} \times t \qquad \text{and} \quad \frac{1}{2} \leq r < 1,\ \dot{E}_{\mathsf{nn}} > 0 \ \text{ kept constant} \tag{27}$$

The strain-rate triaxiality reads

$$\eta_{\dot{\boldsymbol{E}}} = \frac{1+2r}{2(1-r)}$$

Note that since the loading is proportional, the strain-rate triaxiality corresponds exactly to the strain triaxiality $\eta_{\boldsymbol{E}} = E_{\mathsf{m}}/E_{\mathsf{eq}}$. Prescribing the value of $r = -1/2,\ -1/3,\ 0,\ 1/2,\ 2/3$ corresponds to an imposed strain triaxiality $\eta_{\boldsymbol{E}} = 0,\ 0.125,\ 0.5,\ 2,\ 3.5$. The evolution of the normal cohesive stress R_{n}/σ_0 (or Σ_{nn}/σ_0) with respect to the normal opening $[u_{\mathsf{n}}]/h$ (or equivalently with respect to the strain component E_{nn}) is plotted in Figure 2 (left) for the cohesive model and for a GTN material point under various strain triaxialities. The response of the GTN material point has been evaluated using the implicit algorithm of [44] dedicated to a class of pressure-dependent plasticity models.

These curves represent the cohesive traction–separation response corresponding to a unit cell made of a GTN material with a Swift hardening model. Since no elasticity is incorporated in the cohesive model at this stage, the corresponding traction-separation law is *extrinsic*, by opposition to *intrinsic* models where the cohesive response has an initial slope. Contrarily, the GTN material point response presents an initial slope because elasticity has been taken into account in the resolution of the GTN model. This explains the slight difference between the cohesive model and the GTN material point responses particularly highlighted for $\eta_{\boldsymbol{E}} = 0.125$ in Figure 2. Here, in the cohesive model, no crack tip opening is observed as long as the cohesive stress does not reach a given threshold. When the strain triaxiality is vanishing, this threshold is lower than the yield stress of the underlying matrix σ_0. This threshold is about $3-4$ times the yield stress when the strain triaxiality is larger than 0.1. Roughly speaking, for non vanishing strain triaxiality, if a ductile cohesive zone has a toughness R_0, the surface damage occurs when the remote loading reaches about $R_0/3$ or $R_0/4$. This simple result is compatible with other numerical observations [45].
Moreover, when the damage occurs, the cohesive stress decreases rapidly with respect to the crack opening and the ductile CZM is rather brittle for such non vanishing strain triaxiality. The cohesive ductility decreases when the strain triaxiality increases.

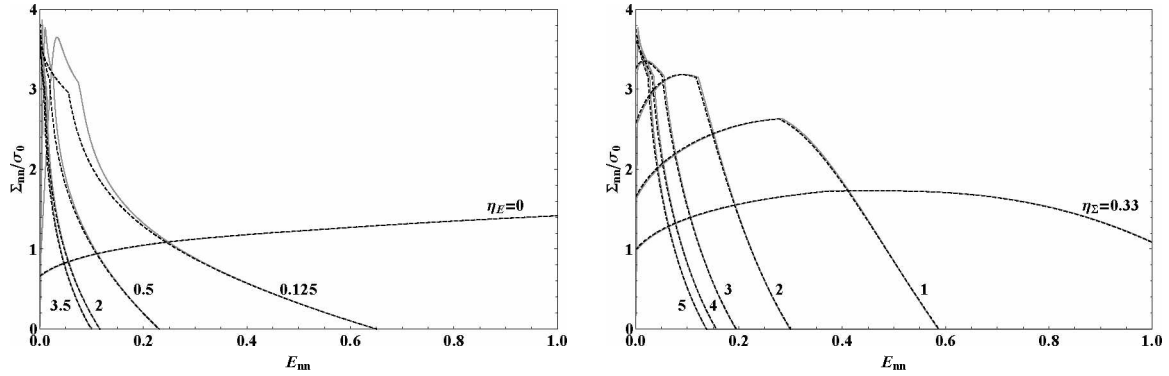

Figure 2: Response of the cohesive model (dashed line) and a GTN material point (solid line) for (left) various strain triaxilities (axisymmetric strain) and (right) various stress triaxilities (axisymmetric stress).

Second, let us consider a prescribed direction of axisymmetric stress:

$$\boldsymbol{\Sigma}(t) = k(t)\,\boldsymbol{\Sigma}^o = k(t)\begin{bmatrix} 1 & 0 & 0 \\ 0 & r^* & 0 \\ 0 & 0 & r^* \end{bmatrix} \qquad \text{and } \frac{1}{2} \leq r^* < 1 \text{ kept constant} \tag{28}$$

where $\boldsymbol{\Sigma}^o$ is a known tensor prescribing the direction of the stress, $k(t)$ is an unknown scalar defining the amplitude of the stress. The procedure of [46] is applied. It consists in finding $\boldsymbol{E}(t)$ and $k(t)$ from the following set of equations:

$$\begin{cases} \boldsymbol{\Sigma}(t) = k(t)\boldsymbol{\Sigma}^o & \text{constitutive equations} \\ \boldsymbol{\Sigma}^o : \boldsymbol{E}(t) = x \end{cases} \tag{29}$$

where x is a prescribed loading parameter. Here, a constant and positive value is prescribed for $\dot{x}$ and the evolution for the loading parameter is $x = \dot{x}\,t$. The stress triaxiality reads

$$\eta_{\boldsymbol{\Sigma}} = \frac{\Sigma_{\mathsf{m}}}{\Sigma_{\mathsf{eq}}} = \frac{1+2r^*}{3(1-r^*)}$$

Since the stress is imposed to be axisymmetric, the strain is also axisymmetric. Moreover, the stress triaxiality $\eta_{\boldsymbol{\Sigma}}$ is prescribed. At the beginning of each time step, the value of E_{nn} is increased and the increment δE_{nn} reads $E_{\mathsf{nn}} - E_{\mathsf{nn}}^{(t-\delta t)}$. The increment of p (or E_{tt}), denoted by δp, is searched such that:

$$\eta_{\boldsymbol{\Sigma}} = \frac{1}{q_2}\frac{H\left(\eta_{\delta\boldsymbol{E}}, q_1 f^*\left(f^{(t-\delta t)}\right)\right)}{D\left(\eta_{\delta\boldsymbol{E}}, q_1 f^*\left(f^{(t-\delta t)}\right)\right)} \quad \text{with} \quad \eta_{\delta\boldsymbol{E}} = \frac{(\delta\boldsymbol{E})_{\mathsf{m}}}{(\delta\boldsymbol{E})_{\mathsf{eq}}} \tag{30}$$

Equation (30) is solved by using a Newton-Raphson algorithm, leading to an updated value for $\eta_{\delta\boldsymbol{E}}$. The value of δp can thus be calculated by relationships presented in Appendix A, leading to an updated value for p. This is performed at the beginning of each time step of the explicit integration scheme presented in subsection 2.4. The evolution of R_{n}/σ_0 as a function of E_{nn} (or $[u_{\mathsf{n}}]/h$) from the cohesive model is plotted in Figure 2 (right) for various stress triaxialities. Again, the corresponding cohesive response is *extrinsic* and the cohesive ductility decreases when the strain triaxiality increases, but the cohesive model appears more ductile for this type of loadings. The peak stress is higher than the initial cohesive thershold and corresponds to the critical porosity f_c.

For both type of loadings, Figure 2 illustrates the high impact of the stress and strain triaxialities on the evolution of the normal cohesive stress. The cohesive strength and the cohesive energy (area under the curve) are strongly dependent on the strain and stress triaxialities, Figure 3. The greater the strain triaxiality, the brittle the cohesive zone: the strength increases with respect to the strain triaxiality while the cohesive energy decreases. Same type of results were already pointed out by [31] and as expected, damage is hard to

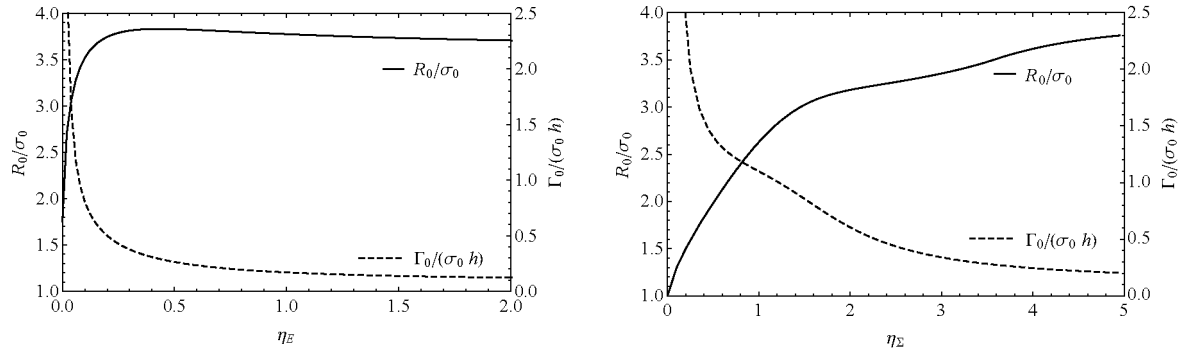

Figure 3: Dependence of the cohesive strength (left axis, black line) and of the cohesive energy (right axis, dashed line) on the strain triaxiality $\eta_{\boldsymbol{E}}$ (Left) or on the stress triaxiality $\eta_{\boldsymbol{\Sigma}}$ (Right).

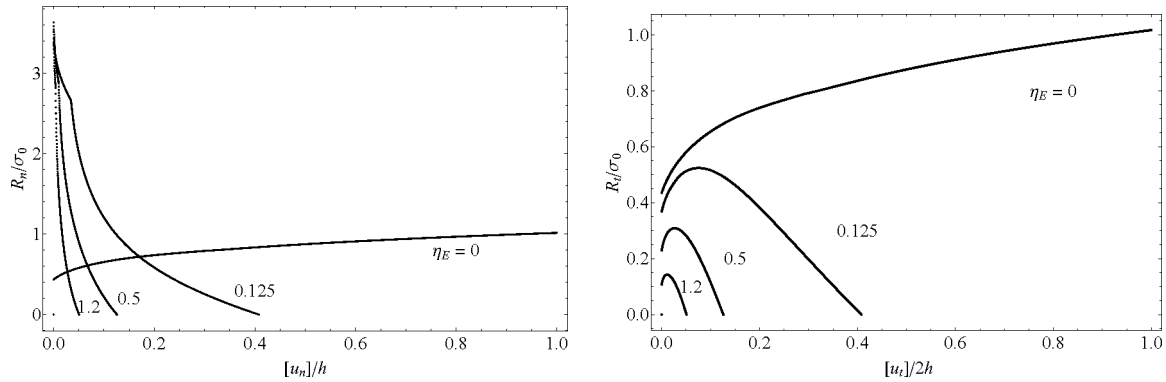

Figure 4: Response of the cohesive model under a mixed mode loading (31) for various strain triaxialities.

develop at very low triaxiality. The maximal normal stress that the cohesive zone can tolerate is reached for a strain triaxiality about 1/2. This lack of damage for low triaxiality loadings is a limitation of the original Gurson model. Nevertheless, note that the model can predict damage for intermediate triaxiality loadings with shear. To illustrate this point, let us consider the following loading combining a normal separation $[u_{\mathbf{n}}]$ and a tangential separation $[u_{\mathbf{t}}]$ (with $E_{\mathbf{nn}} = [u_{\mathbf{n}}]/h$ and $E_{\mathbf{nt}} = [u_{\mathbf{t}}]/(2h)$):

$$\boldsymbol{E} = \begin{bmatrix} \dot{E} & \dot{E} & 0 \\ \dot{E} & r\,\dot{E} & 0 \\ 0 & 0 & r\,\dot{E} \end{bmatrix} \times t \qquad \text{with} \quad \dot{E} > 0 \ \text{ kept constant} \tag{31}$$

Prescribing the value of $r = -0.5,\ -0.23,\ 0.4,\ 1.8$ corresponds to an imposed strain triaxiality $\eta_{\boldsymbol{E}} \approx 0,\ 0.125,\ 0.5,\ 1.2$. The evolution of $R_{\mathbf{n}}/\sigma_0$ (or $R_{\mathbf{t}}/\sigma_0$) as a function of $[u_{\mathbf{n}}]/h$ (or $[u_{\mathbf{t}}]/(2h)$) from the cohesive model is plotted in Figure 4. Imposing a tangential separation leads to a non-zero tangential stress vector which exhibits damage for intermediate triaxialities.

Again, note that there is no fitting parameter in the obtained cohesive model. Once the GTN parameters are known, the cohesive model is fully defined. This is a major feature of the proposed cohesive model.

3. Numerical implementation into a cohesive-volumetric finite element formulation

The numerical simulations are performed using the XPER software dedicated to the simulation of fracture dynamics of heterogeneous materials [47, 48]. This computer code proposes a periodic homogenization framework under small or finite strain theories, but it can also be used for more general structure computations. XPER implementation involves a multi-contact modeling strategy based on the Non-Smooth Contact

Dynamics (NSCD) method where cohesive models are introduced as mixed boundary conditions between each volumetric finite element. Each element or either a group of elements of the mesh can be considered as an independent body and the interface between bodies follows a frictional CZM with no regularization nor penalization. CZM are introduced by a slight modification of Signorini-Coulomb conditions [45, 49]. The bulk behavior inside each element corresponds to a hardening behavior without any damage. The damage is modeled at the interface between bodies by the cohesive law. Moreover, the NSCD method avoids instabilities arising with softening models, see [45, 50] for details.

For the numerical implementation, one has first to specify how the variable $\dot{p}$ is updated during the computation. Then, some changes have been performed regarding the cohesive zone model. Indeed, as XPER typically uses *intrinsic* cohesive zone models, a modification of the cohesive model is proposed hereafter to change it from extrinsic to intrinsic. Furthermore, as in a fully general structure computation the loading may be followed by an unloading situation, it has to be introduced in the cohesive model. Thus, the cohesive model is enriched to ensure that the unloading case is properly handled. Finally, the model has been implemented under the assumption of proportional loading and the cohesive stress given by (25) is estimated using the total cohesive strain $\boldsymbol{E}$ instead of the strain increment tensor $\delta\boldsymbol{E}$. As in the deformation theory, this approach is valid under the restrictive case of a monotonous and proportional loading, but from numerical standpoint allows a simpler numerical integration of the cohesive model.

3.1. Estimate of the in-plane strain rate $\dot{p}$

The strain rate $\dot{p}$ is estimated by considering information coming from the volumetric elements adjacent to the cohesive zone. Among several possibilities, it is chosen here to compute $\dot{p}$ by maintaining the equality between the strain-rate triaxiality $\eta_{\dot{\boldsymbol{E}}}$ in the cohesive zone and the strain-rate triaxiality $\eta^{\mathsf{vol}}_{\dot{\boldsymbol{E}}}$ computed from the stress state in a volumetric element adjacent to the cohesive zone. From the normality rule, GTN model leads to:

$$\dot{\boldsymbol{E}} = \dot{\lambda}\left(\frac{q_1 q_2 f^*}{\sigma_y}\sinh\left(\frac{3}{2}q_2\frac{\Sigma_{\mathsf{m}}}{\sigma_y}\right)\boldsymbol{i} + \frac{3}{\sigma_y^2}\boldsymbol{\Sigma}^{\mathsf{d}}\right) \quad \text{with} \quad \dot{\lambda} > 0 \tag{32}$$

Substituting in this expression the average stress tensor over the volumetric slave element (denoted by $\boldsymbol{\Sigma}^{\mathsf{vol}}$) adjacent to the cohesive zone, the corresponding strain rate triaxiality reads

$$\eta^{\mathsf{vol}}_{\dot{\boldsymbol{E}}} = \frac{q_1 q_2 f^* \sinh\left(\frac{3}{2}q_2\frac{\Sigma^{\mathsf{vol}}_{\mathsf{m}}}{\sigma_y}\right)}{2\frac{\Sigma^{\mathsf{vol}}_{\mathsf{eq}}}{\sigma_y}} \tag{33}$$

From (15), the strain-rate triaxility in the cohesive zone reads:

$$\eta_{\dot{\boldsymbol{E}}} = \frac{\frac{[\dot{u}_{\mathsf{n}}]}{h} + 2\dot{p}}{2\sqrt{\left(\frac{[\dot{u}_{\mathsf{n}}]}{h} - \dot{p}\right)^2 + \frac{3}{4}\frac{[\dot{u}_{\mathsf{t}}]^2}{h^2} + \frac{3}{4}\frac{[\dot{u}_{\mathsf{s}}]^2}{h^2}}} \tag{34}$$

By equating (33) and (34) the strain rate $\dot{p}$ is determined. It appears that $\dot{p}$ evolves as a function of the cohesive kinematics and the stress state of the adjacent volumetric slave element. Only the case $[\dot{u}_{\mathsf{n}}] > 0$, corresponding to a positive loading, is considered here (the unloading case $[\dot{u}_{\mathsf{n}}] < 0$ will be separately treated in section 3.3) and different expressions for $\dot{p}$ are determined (see Appendix A for a detailed description). The selected expressions are reported in Table 2.

From the C(T) test simulations presented in section 4, it was observed that the resulting triaxiality $\eta^{\mathsf{vol}}_{\dot{\boldsymbol{E}}}$ decreases when increasing the damage in the cohesive zone. Since the model does not predict any damage for low triaxiality, the rupture is artificially delayed. To address this issue, the volumetric stress $\boldsymbol{\Sigma}^{\mathsf{vol}}$ is transferred to the cohesive zone up to the onset of coalescence (when f reaches f_c). Over the void coalescence, the value of $\boldsymbol{\Sigma}^{\mathsf{vol}}$ is kept constant during the post-coalescence stage and the stress triaxiality does not evolve anymore, see Figure 9 in the sequel.

$\eta_{\dot{\boldsymbol{E}}}^{\mathsf{vol}}$	$\dot{p}([\dot{\boldsymbol{u}}], \eta_{\dot{\boldsymbol{E}}}^{\mathsf{vol}})$
$\eta_{\dot{\boldsymbol{E}}}^{\mathsf{vol}} < 0$	$\dot{p} = -\dfrac{[\dot{u}_{\mathsf{n}}]}{2h}$
$0 \leq \eta_{\dot{\boldsymbol{E}}}^{\mathsf{vol}} < 1$ and $\eta_{\dot{\boldsymbol{E}}}^{\mathsf{vol}} > 1$	$\dot{p} = \dfrac{2\left(\eta_{\dot{\boldsymbol{E}}}^{\mathsf{vol}}\right)^2 + 1}{2\left(\left(\eta_{\dot{\boldsymbol{E}}}^{\mathsf{vol}}\right)^2 - 1\right)} \dfrac{[\dot{u}_{\mathsf{n}}]}{h} - \dfrac{\left\lvert \eta_{\dot{\boldsymbol{E}}}^{\mathsf{vol}} \right\rvert \sqrt{9\dfrac{[\dot{u}_{\mathsf{n}}]^2}{h^2} + 3(1 - \left(\eta_{\dot{\boldsymbol{E}}}^{\mathsf{vol}}\right)^2)\left(\dfrac{[\dot{u}_{\mathsf{t}}]^2}{h^2} + \dfrac{[\dot{u}_{\mathsf{s}}]^2}{h^2}\right)}}{2\left(\left(\eta_{\dot{\boldsymbol{E}}}^{\mathsf{vol}}\right)^2 - 1\right)}$
$\eta_{\dot{\boldsymbol{E}}}^{\mathsf{vol}} = 1$	$\dot{p} = \dfrac{1}{4}\dfrac{[\dot{u}_{\mathsf{n}}]^2 + [\dot{u}_{\mathsf{t}}]^2 + [\dot{u}_{\mathsf{s}}]^2}{[\dot{u}_{\mathsf{n}}]h}$

Table 2: Expressions of in-plane strain rate components $\dot{p}$ depending on crack tip opening rate $[\dot{\boldsymbol{u}}]$ and surrounding volumetric strain rate triaxiality $\eta_{\dot{\boldsymbol{E}}}^{\mathsf{vol}}$.

3.2. Intrinsic cohesive zone model

We propose here a simple manner to convert an extrinsic CZM to an intrinsic one. The stress vector $\boldsymbol{R}$ is multiplied by a positive increasing function that rapidly tends to 1 with respect to the crack opening. The resulting stress vector is denoted by $\boldsymbol{R}^{(\mathsf{int})}$:

$$\boldsymbol{R}^{(\mathsf{int})} = \begin{cases} R_n^{(\mathsf{int})} = \left(1 - \exp\left(-\alpha_{\mathsf{n}} \dfrac{[u_{\mathsf{n}}]}{h}\right)\right) \times R_{\mathsf{n}} \\ R_t^{(\mathsf{int})} = \left(1 - \exp\left(-\alpha_{\mathsf{t}} \dfrac{|[u_{\mathsf{t}}]|}{h}\right)\right) \times R_{\mathsf{t}} \\ R_s^{(\mathsf{int})} = \left(1 - \exp\left(-\alpha_{\mathsf{s}} \dfrac{|[u_{\mathsf{s}}]|}{h}\right)\right) \times R_{\mathsf{s}} \end{cases} \tag{35}$$

The initial stiffness is calibrated through the parameters α_{n}, α_{t}, and α_{s} that have been calculated with the help of equations (B.4), (B.8) and (B.9) given in Appendix B.

3.3. Unloading case

Since local unloading can occur during a crack growth in a fully general structure computation, one need to specify the behavior of the cohesive zone model during unloading taking into account the irreversibility of the damage process.

A criterion has to be defined to distinguish loading state and unloading state. It is chosen to handle the unloading in each direction separately. It means that an unloading can occur in one direction while the other directions are still loaded. In the normal direction, unloading occurs if:

$$[u_{\mathsf{n}}]^{(t)} - [u_{\mathsf{n}}]^{(t-\delta t)} < 0 \tag{36}$$

For the tangential directions, unloading occurs respectively in $\boldsymbol{t}$ or $\boldsymbol{s}$ directions if:

$$|[u_{\mathsf{t}}]^{(t)}| - |[u_{\mathsf{t}}]^{(t-\delta t)}| < 0 \qquad \text{or} \qquad |[u_{\mathsf{s}}]^{(t)}| - |[u_{\mathsf{s}}]^{(t-\delta t)}| < 0 \tag{37}$$

One has also to define the behavior of the cohesive zone during unloading. The maximum values of separation in each direction that have occurred during the loading process are introduced to take into account the loading history in the cohesive zone and the irreversibility of the damage process

$$[u_i]_{\mathsf{max}} = \max_{0 \leq \tau \leq t} |[u_i](\tau)| \quad \text{with } i = \mathsf{n}, \mathsf{t}, \mathsf{s} \tag{38}$$

Following [51], the unloading behavior is assumed to be an elastic unloading up to the origin and a further elastic reloading also:

$$\bar{\boldsymbol{R}} = \left(R_{\mathsf{n}}^{(\mathsf{int})}\right)_{\mathsf{max}} \frac{[u_{\mathsf{n}}]}{[u_{\mathsf{n}}]_{\mathsf{max}}} \boldsymbol{n} + \left(R_{\mathsf{t}}^{(\mathsf{int})}\right)_{\mathsf{max}} \frac{[u_{\mathsf{t}}]}{[u_{\mathsf{t}}]_{\mathsf{max}}} \boldsymbol{t} + \left(R_{\mathsf{s}}^{(\mathsf{int})}\right)_{\mathsf{max}} \frac{[u_{\mathsf{s}}]}{[u_{\mathsf{s}}]_{\mathsf{max}}} \boldsymbol{s} \tag{39}$$

where the $\left(R_i^{(\mathsf{int})}\right)_{\mathsf{max}}$ are the components of the cohesive stress $\boldsymbol{R}^{(\mathsf{int})}$ evaluated at the maximal opening $[u_i]_{\mathsf{max}}$, $i = \mathsf{n}, \mathsf{t}, \mathsf{s}$. The unloading rule described in (39) is illustrated in Figure 5. For sake of simplicity, the stress vector $\bar{\boldsymbol{R}}$ is simply denoted by $\boldsymbol{R}$ in Figure 5 and in the next section. The unloading behavior is then completed by assuming the irreversibility of the damage and the hardening during the loading process:

$$\forall \tau \in [0,t], \quad \dot{f}(\tau) \geq 0 \quad \text{and} \quad \dot{\bar{\varepsilon}}(\tau) \geq 0 \tag{40}$$

From a practical point of view, two additional tests are performed in the integration scheme to meet the conditions (40):

$$\text{if} \quad f < f^{(t-\delta t)} \quad \text{then} \quad f = f^{(t-\delta t)} \qquad \text{and} \qquad \text{if} \quad \bar{\varepsilon} < \bar{\varepsilon}^{(t-\delta t)} \quad \text{then} \quad \bar{\varepsilon} = \bar{\varepsilon}^{(t-\delta t)} \tag{41}$$

The general equations of the cohesive zone model are summarized in Appendix C. It is worth noting that this elastic unloading is not really realistic. During an unloading voids closure can occur involving some compressive plastic effects. This effect is not taken into account here but a simple elastic unloading allows to avoid spurious effects when unloading of CZM arises.

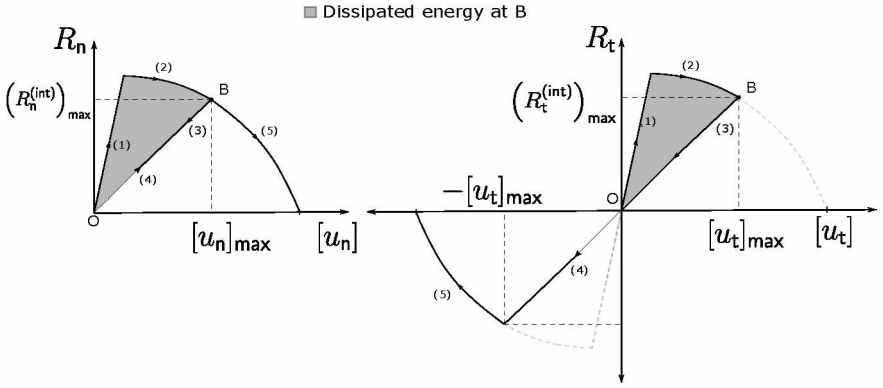

Figure 5: Illustration of the unloading rule. (1) initial loading, (2) loading (softening), (3) unloading, (4) reloading, (5) loading (softening). (a) normal direction, (b) tangential direction.

4. Application: simulation of compact tensile tests

The cohesive zone model is applied to simulate crack growth in a compact tension C(T) specimen under the plane strain conditions. The objective here is to illustrate the ability of the new cohesive zone model to simulate crack growth. Full 3D simulations are left for future work. The material under consideration is a ferritic steel StE460 (German designation) for which experimental data of crack growth tests and parameters for the GTN model have already been reported in many works [30, 32, 52, 53]. The material parameters are reported in Table 1. The material surrounding the cohesive zones is an elastic-plastic solid with hardening law (26), identical to the matrix surrounding the voids in the GTN analysis.
A material length scale of $\Lambda = 200\ \mu m$ has been used with these material properties in [32, 53], as a typical value for the ductile fracture in ferritic steels. In these papers, the numerical simulations are performed on one half of the specimen making use of the symmetry boundary conditions. The cohesive properties (energy Γ_0 and strength R_0) used to model the half of the process zone were calibrated on a single element of size $\Lambda \times \Lambda$ with the GTN model representing a unit cell of material. Thus, the total cohesive energy per crack increment is $2\Gamma_0$. Here, the numerical simulations are performed on a full specimen and since the dissipated energy in a single element is proportional to the size of the element, the parameter h is chosen as the size of a square cell of area $2\Lambda^2$, with $h = \sqrt{2} \times 200\ \mu m$, here overestimated by $h \approx 300\ \mu m$. The C_{n} and C_{t} parameters are set to $10^{18}\ Pa/m$ in order to respect the criterion $C_{\mathsf{n}} = C_{\mathsf{t}} > 21Y/l_{\mathsf{mesh}}$ theoretically derived

l_{mesh}	number of elements in the central zone	total number of elements
200 μm	1600	20220
150 μm	2809	26198
100 μm	6400	38020
50 μm	25000	112638

Table 3: Mesh size and number of elements

by [54] even for the smallest mesh size used in this paper $l_{\mathsf{mesh}} \approx 50\,\mu m$.
The dimensions of the standard C(T) side-grooved specimen used for the tests are: $W = 50\ mm$ (width), $a_0/W = 0.59$ (initial relative crack length), $B = 25\ mm$ (thickness), $B_n = 19\ mm$ (net thickness between side grooves). The experimental so-called R-Curve in terms of $J - \Delta a$ from these tests are reported in [30, 32, 52, 53].
The simulations are performed with two-dimensional 4 nodes linear plane strain $Q1$ elements and two contact nodes per cohesive zones are introduced (no significant interpenetration even in case of local rotation). The specimen is located in the x-y plane. The finite element mesh is depicted on Figure 6. Since the crack path is known, cohesive zones are only put along the line in front of the crack tip, assuming pure mode I crack propagation. The model thus contains a series of cohesive elements located along a line in front of the crack tip which is taken to be initially sharp. The mesh is refined in front of the crack tip, over an initial surface $8\,mm \times 8\,mm$, and the bulk elements in this central zone have the initial dimension $l_{\mathsf{mesh}} \times l_{\mathsf{mesh}}$. A coarser mesh is used out of this zone. Information concerning the mesh are specified in Table 3. The two circular holes are partially filled with a purely elastic material (same Young modulus and Poisson ratio as specified in Table 1) in order to apply the loading without any bias on the local shear stress. The loading consists in imposing the vertical component along the y axis of the velocity to $\dot{U}_y$ for the upper part of the specimen and to $-\dot{U}_y$ for the lower part of the specimen. The calculation are made using an explicit finite element solver with an implicit contact resolution, see [48] for details. Since softening behaviors induce instabilities, a dynamical formulation is here employed, again see [48]. This formulation however requires very small time steps (δt about $10^{-9}\,s$ to $10^{-8}\,s$). Since instantaneous behavior laws are invoked, a high velocity is prescribed ($\dot{U}_y = 0.1\,m.s^{-1}$) in order to counterbalance the small time step and run the simulations in a reasonable time. The mass density of the material is set to $7.8 \times 10^3\,kg/m^3$.

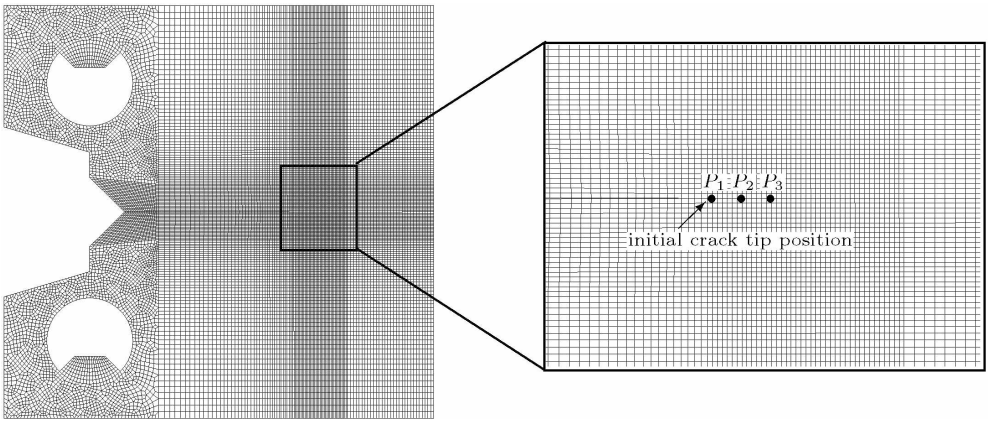

Figure 6: C(T) specimen mesh with mesh size at the crack tip $l_{\mathsf{mesh}} = 200\,\mu m$. Three positions ahead of the crack tip: P_1 at initial crack tip, P_2 one millimeter ahead, P_3 two millimeter ahead.

4.1. Results

The numerical overall response of the C(T) is compared in Figure 7 (left) to experimental data of [55]. Since the simulations are computed in 2D under plane strain assumption and the specimen is side grooved,

the effective thickness $B_{\text{eff}} = \sqrt{B \times B_n}$ is considered for the calculation of the resulting forces, see [55]. The overall agreement is good since *there is no parameter to adjust*. The crack growth resistance curve is also well predicted. The J-integral versus crack extension Δa is evaluated using ASTM E1820 formula [56] and compared to experimental data of [30] in Figure 7 (right). The numerical model is found to be in reasonable accordance with the experiments.

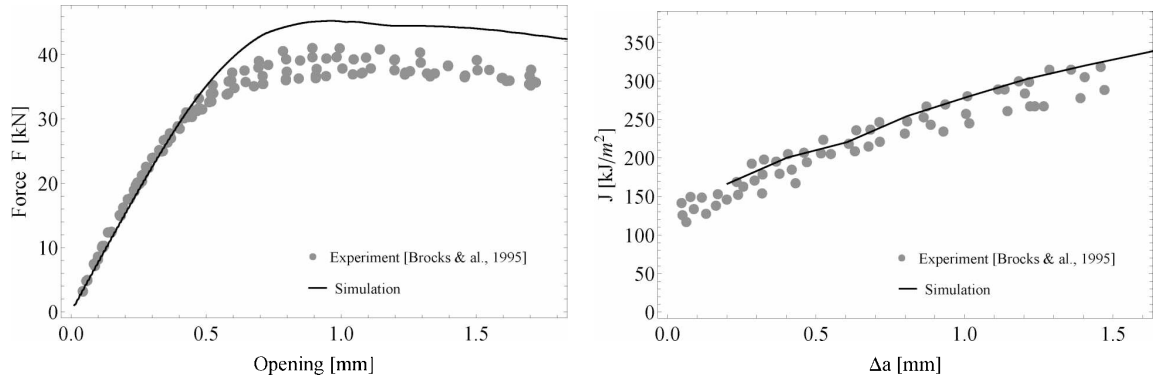

Figure 7: Cohesive-Volumetric finite element simulation (thick lines) vs experiments (gray points). (Left) Overall response: Load F vs opening displacement v, experiments of [55]. (Right) Crack growth resistance curve: J-integral vs crack extension Δa, experiments of [55].

During the crack propagation, plasticity develops in the vicinity of the crack tip where tension occurs and at the free boundary ahead of the crack tip where intense compressible loadings are supported, see Figure 8. The von Mises stress field and the cumulated plastic strain field thus exhibit non trivial spatial structures in the vicinity of the crack tip. The resulting stress and strain triaxiality fields also exhibit complex spatial structure.

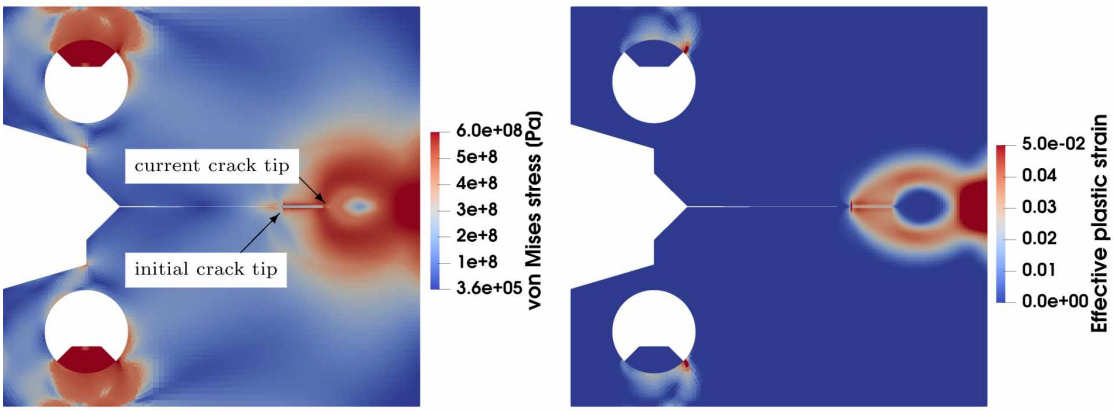

Figure 8: Equivalent von Mises stress field (left) and cumulated plastic strain field (right) at crack length $\Delta a = 6\ mm$.

As expected, the local CZM that drives the crack propagation depends on this spatial distribution of the triaxiality fields and thus on the position ahead of the crack tip, Figure 9. Since the evolution of local stress triaxiality with respect to the overall loading is not the same at point P_1 where the crack propagation initiates than at point P_2 where the crack propagation reaches a steady state, the associated local cohesive response is also not the same. Point P_3 is in the same steady state as point P_2, its local response is the same as P_2 and thus not plotted on the figure. It is readily to see that more cohesive energy is needed to

initiate the crack propagation than to propagate it in a steady state. Note that the simulations of [21] for analyzing the mode I crack advance initiating from a pre-crack in a large scale plate structure led to the opposite trend. The plate was modeled with shell elements and nodal spring-type cohesive elements were used along the crack path. They obtained a relatively small cohesive energy for elements immediately ahead of the pre-crack tip. Thus the result obtained in the present paper must be dependent of the plane strain conditions. A full study with a comparison between 2D plane strain, 2D plane stress and 3D simulations would be required to discuss this point in depth. It is also worth noting that the shape of the local cohesive response is not *a priori* given and arises from the loading and the micromechanical model. It is again a significant feature of the model. At the crack onset, the CZM is rather a door-like model, while it looks like a triangular one during crack propagation. The peak stress stays about 3 times of the yield stress.

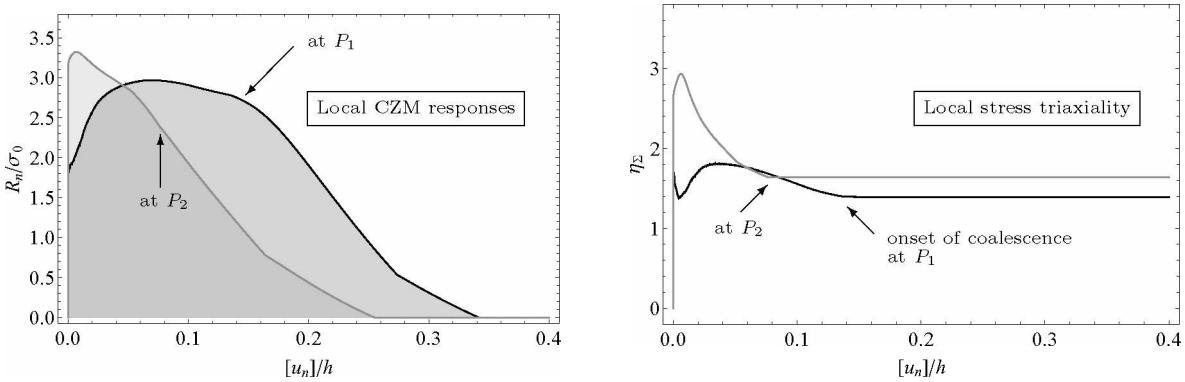

Figure 9: The local cohesive responses at point P_1 (initial crack tip) and P_2 (1 mm ahead of the crack tip) are different (left) since the local stress triaxiality $\eta_{\mathbf{\Sigma}}$ does not evolve as the same manner at these points during the macroscopic loading (right). The stress triaxiality is fixed to a constant value at the onset of coalescence.

Coherence of the results can be reinforced with the help of a simple estimate. Focusing on Figure 9 (b), the stress triaxiality $\eta_{\mathbf{\Sigma}}$ at the crack tip and at the onset of coalescence is about $\eta_{\mathbf{\Sigma}} \simeq 1.4$. For this stress triaxiality value, results obtained in Figure 3 (b) give $\Gamma_0/(\sigma_0 h) \simeq 0.9$. Identifying the mode I cohesive energy Γ_0 to the critical value J_{Ic} of the J-integral and estimating $J_{Ic} \simeq 145 kJ/m^2$ in Figure 7 (b) for a crack extension $\Delta a \simeq 0.2mm$ (see [57]), one obtains $h \simeq 340\mu m$ which is fully consistent with the value used in these calculations ($h = 300\mu m$).

4.2. Length scale parameter and mesh size sensitivity

Figure 10 (left) exhibits the macroscopic response for different values of the length scale parameter h. As expected, the overall response is strengthened when increasing h while keeping mesh size l_{mesh} constant. The parameter h scales the local energy dissipated by the cohesive zones. When h increases it can be considered that the cohesive energy is smeared out over a larger length and the effect of localization decreases.
Contrarily, the overall response is strengthened when decreasing l_{mesh} while keeping length scale parameter h constant, Figure 10 (right). This effect is more unusual since, in the local approach of continuum damage mechanics, the dissipated energy vanishes when the element size tends to zero as a consequence of the damage localization within a single band of elements [58]. Here, the cohesive energy is dissipated along the cohesive zones and not in the bulk elements. A scale effect arises: when the mesh size l_{mesh} decreases, the h-length acts over a larger part of the surrounding finite elements and again, it can be considered that the cohesive energy is smeared out over a larger length.

An artificial hardening is thus obtained when decreasing l_{mesh} while keeping mesh size h constant. This hardening can be counterbalanced by adjusting the value of length scale parameter h with respect to the mesh size l_{mesh}. Figure 11 shows that it is possible to get an overall load-opening response independent on the mesh size if the length scale parameter is set conveniently. The linear fit $h \simeq 220 + 0.4 l_{\mathsf{mesh}}$ (in μm) seems accurate for the current simulations.

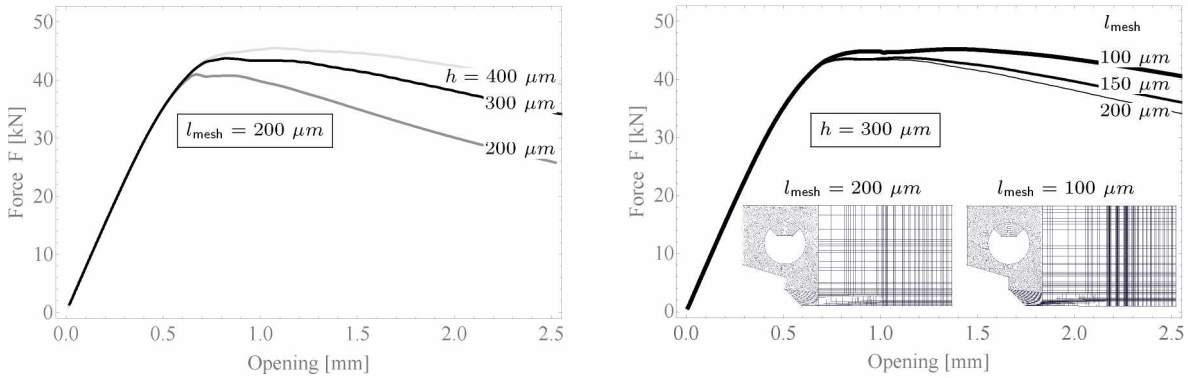

Figure 10: Cohesive-Volumetric finite element simulations, overall load-opening response. Dependence on the thickness parameter for mesh size $l_{\text{mesh}} = 200\ \mu m$ (Left) and dependence on the mesh size for thickness parameter $h = 300\ \mu m$ (Right). Inset: upper part of the corresponding meshes, with mesh refinement in the process zone.

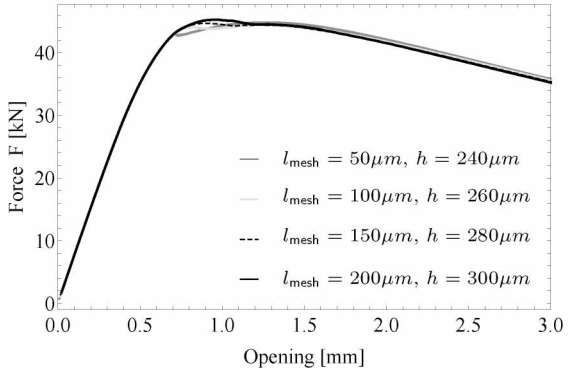

Figure 11: Adapting the length scale parameter h with respect to the mesh size l_{mesh} in order to obtain converged overall load-opening response.

5. Conclusion

In this paper the problem of simulating the crack initiation and growth in ductile materials failing by void nucleation, growth and coalescence is investigated. A crack surface is considered to be a limit case of strain localization band leading to a discontinuity of displacement field. The cohesive-volumetric approach appears to be a suitable framework for the description of discontinuity inside a material. In this framework, the hardening behavior of the material is described by the bulk behavior and the damage is described as a cohesive surface with a corresponding traction–separation law. Since in ductile fracture the material separation depends on the local stress and strain states which are strongly dependent on the geometry, a triaxiality-dependent cohesive model is derived. The cohesive surface is approximated as a band of small thickness whose behavior follows a volumetric GTN model. The obtained traction–separation law is a GTN-like model with reduced kinematics. This approach introduces a regularizing length parameter h whose the link with the physical size of the localization band remains to be investigated. The GTN traction–separation law reproduces the behavior of a single volumetric element made of a GTN material. It accurately captures the stress or strain rate triaxiality dependence but suffers from the same limitation as the GTN model and does not predict any damage at low triaxiality. However the procedure developed is general and could be extended to more sophisticated micro-mechanical model which takes into account damage at low triaxiality or even viscoplastic effects. The application of this approach to simulate crack propagation in a standard compact tension specimen of ferritic steel shows the ability of the cohesive-volumetric approach to simulate crack growth in ductile material. The results are consistent with previous results obtained by

other authors. The application also exhibits the dependence of the regularization parameter h on a material length characterizing the microstructure and the mesh size. The main result of this work is the ability to derive CZM from any softening bulk behavior without any *a priori* assumptions on the shape of the cohesive model. Many previous numerical constatations are here re-obtained with no fitting parameters.

Appendix A. Expressions of $\dot{p}$

First, let us consider the case $\eta_{\boldsymbol{E}}^{\mathsf{vol}} \geq 0$ corresponding to tension. Condition $\eta_{\boldsymbol{E}}^2 = \left(\eta_{\boldsymbol{E}}^{\mathsf{vol}}\right)^2$ leads to the following solutions for $\dot{p}$.

If $\eta_{\boldsymbol{E}}^{\mathsf{vol}} = 1$, the solution is straightforward

$$\dot{p} = \frac{1}{4}\frac{[\dot{u}_{\mathsf{n}}]^2 + [\dot{u}_{\mathsf{t}}]^2 + [\dot{u}_{\mathsf{s}}]^2}{[\dot{u}_{\mathsf{n}}]h} \tag{A.1}$$

If $\eta_{\boldsymbol{E}}^{\mathsf{vol}} \neq 1$,

$$\dot{p}_{\pm} = \frac{2\left(\eta_{\boldsymbol{E}}^{\mathsf{vol}}\right)^2 + 1}{2\left(\left(\eta_{\boldsymbol{E}}^{\mathsf{vol}}\right)^2 - 1\right)}\frac{[\dot{u}_{\mathsf{n}}]}{h} \pm \frac{\left|\eta_{\boldsymbol{E}}^{\mathsf{vol}}\right|\sqrt{9\frac{[\dot{u}_{\mathsf{n}}]^2}{h^2} + 3(1-\left(\eta_{\boldsymbol{E}}^{\mathsf{vol}}\right)^2)\left(\frac{[\dot{u}_{\mathsf{t}}]^2}{h^2} + \frac{[\dot{u}_{\mathsf{s}}]^2}{h^2}\right)}}{2\left(\left(\eta_{\boldsymbol{E}}^{\mathsf{vol}}\right)^2 - 1\right)} \tag{A.2}$$

For $0 \leq \eta_{\boldsymbol{E}}^{\mathsf{vol}} < 1$, it appears that the negative branch should be selected, using the inequalities:

$$\dot{p} \geq -[\dot{u}_{\mathsf{n}}]/(2h), \qquad \frac{2\left(\eta_{\boldsymbol{E}}^{\mathsf{vol}}\right)^2 + 1}{2(\left(\eta_{\boldsymbol{E}}^{\mathsf{vol}}\right)^2 - 1)} \leq -1/2, \qquad \left(\eta_{\boldsymbol{E}}^{\mathsf{vol}}\right)^2 - 1 < 0$$

For $\eta_{\boldsymbol{E}}^{\mathsf{vol}} > 1$, considering that the normal strain rate in the cohesive zone $[\dot{u}_{\mathsf{n}}]/h$ should be greater than the transverse strain rate $\dot{p}$, it appears from (A.2) that the negative branch should also be selected (using the inequalities: $[2\left(\eta_{\boldsymbol{E}}^{\mathsf{vol}}\right)^2 + 1]/[2(\left(\eta_{\boldsymbol{E}}^{\mathsf{vol}}\right)^2 - 1)] > 1$ and $\left(\eta_{\boldsymbol{E}}^{\mathsf{vol}}\right)^2 - 1 > 0$).

Secondly, let us consider the case $\eta_{\boldsymbol{E}}^{\mathsf{vol}} < 0$ corresponding to a compression state. The evolution law of the porosity (19) indicates that the porosity is decreasing. Keeping in mind that the damage variable can only be a growing function, it is chosen here to determine $\dot{p}$ from the zero triaxiality $\eta_{\boldsymbol{E}}^{\mathsf{vol}} = 0$. It leads to:

$$\dot{p} = -\frac{[\dot{u}_{\mathsf{n}}]}{2h} \tag{A.3}$$

Appendix B. Expressions of α_{n}, α_{t}, and α_{s}

The initial slope of the function $R^{(\mathsf{int})}$ is typically denoted by C_{n} in the normal direction and $C_{\mathsf{t}} = C_{\mathsf{s}}$ in the tangential directions. It is known that the insertion of intrinsic cohesive models into finite element meshes leads to an additional compliance in the overall force-displacement response. Therefore, the cohesive stiffness has to be set high enough to avoid additional compliance in the material, but not too large in other to avoid numerical instabilities. Various criteria are available to calibrate the cohesive stiffness for given material properties and a given mesh [59–61]. Here, parameters α_{n}, α_{t} and α_{s} are expressed in terms of C_{n} and C_{t}. By doing so, existing criteria derived for C_{n} and C_{t} can be directly used to adjust α_{n}, α_{t} and α_{s}.

Let us consider a simple case of uniaxial tensile loading with no hardening ($\sigma_y = \sigma_0$):

$$\boldsymbol{E} = \begin{bmatrix} \dot{E}_{\mathsf{nn}} & 0 & 0 \\ 0 & 0 & 0 \\ 0 & 0 & 0 \end{bmatrix} \times t, \qquad \text{and } \dot{E}_{\mathsf{nn}} > 0 \text{ kept constant} \tag{B.1}$$

In this case, the normal stress vector reads:

$$R_{\mathsf{n}}^{(\mathsf{int})} = \sigma_0 \left(\frac{1}{q_2} H(\frac{1}{2}, q_1 f^*) + \frac{2}{3} D(\frac{1}{2}, q_1 f^*) \right) \left(1 - \exp\left(-\alpha_{\mathsf{n}} \frac{[u_{\mathsf{n}}]}{h} \right) \right) \tag{B.2}$$

By imposing:

$$\frac{\partial R_{\mathsf{n}}^{(\mathsf{int})}}{\partial [u_{\mathsf{n}}]} \left([u_{\mathsf{n}}] = 0 \right) = C_{\mathsf{n}} \tag{B.3}$$

the parameter α_{n} reads:

$$\alpha_{\mathsf{n}} = \frac{C_{\mathsf{n}}\, h}{\sigma_0 \left(\frac{1}{q_2} H(\frac{1}{2}, q_1 f^*(f_0)) + \frac{2}{3} D(\frac{1}{2}, q_1 f^*(f_0)) \right)} \tag{B.4}$$

This expression is used in the numerical simulations (section 4) to estimate α_{n}. A similar approach can be followed to estimate α_{t}. Let us consider a simple case of pure shear loading with no hardening ($\sigma_y = \sigma_0$):

$$\boldsymbol{E} = \begin{bmatrix} 0 & \dot{E}_{\mathsf{nt}} & 0 \\ \dot{E}_{\mathsf{nt}} & 0 & 0 \\ 0 & 0 & 0 \end{bmatrix} \times t \qquad \text{and } \dot{E}_{\mathsf{tt}} > 0 \text{ kept constant} \tag{B.5}$$

In this case, the tangential stress vector reads:

$$R_t^{(\mathsf{int})} = \sigma_0 \frac{1}{\sqrt{3}} (1 - q_1 f^*) \left(1 - \exp\left(-\alpha_{\mathsf{t}} \frac{||[u_{\mathsf{t}}]||}{h} \right) \right) \tag{B.6}$$

By imposing:

$$\frac{\partial R_t^{(\mathsf{int})}}{\partial [u_{\mathsf{t}}]} \left([u_{\mathsf{t}}] = 0 \right) = C_{\mathsf{t}} \tag{B.7}$$

the parameter α_{t} reads:

$$\alpha_{\mathsf{t}} = \frac{\sqrt{3}\, C_{\mathsf{t}}\, h}{\sigma_0 (1 - q_1 f^*(f_0))} \tag{B.8}$$

This expression is used in the numerical simulations (section 4) to estimate α_{t}. A similar expression can be obtained for α_{s} from a C_{s} parameter:

$$\alpha_{\mathsf{s}} = \frac{\sqrt{3}\, C_{\mathsf{s}}\, h}{\sigma_0 (1 - q_1 f^*(f_0))} \tag{B.9}$$

Appendix C. General equations of the cohesive zone model

The general equations used for the numerical implementation of the cohesive model are summarized below.

For each time t, the opening vector ($[u_{\mathsf{n}}]$, $[u_{\mathsf{t}}]$, $[u_{\mathsf{s}}]$) is known and the maximal values are updated:

$$[u_i]_{\mathsf{max}} = \max_{0 \le \tau \le t} |[u_i](\tau)| \quad \text{with } i = \mathsf{n}, \mathsf{t}, \mathsf{s} \tag{C.1}$$

The following quantities are computed from the maximal openings:

$$\epsilon_{\mathsf{nn}} = \frac{[u_{\mathsf{n}}]_{\mathsf{max}}}{h}, \quad \epsilon_{\mathsf{nt}} = \frac{[u_{\mathsf{t}}]_{\mathsf{max}}}{2h}, \quad \epsilon_{\mathsf{ns}} = \frac{[u_{\mathsf{s}}]_{\mathsf{max}}}{2h}$$

The previous values $\epsilon_{\mathsf{nn}}^{(t-\delta t)}$, $\epsilon_{\mathsf{nt}}^{(t-\delta t)}$, $\epsilon_{\mathsf{ns}}^{(t-\delta t)}$, the porosity $f^{(t-\delta t)}$ and the average strain $\bar{\varepsilon}^{(t-\delta t)}$ are known. The differences between two time steps are denoted by a δ (e.g. $\delta\epsilon_{\mathsf{nn}} = \epsilon_{\mathsf{nn}} - \epsilon_{\mathsf{nn}}^{(t-\delta t)}$). If $f^{(t-\delta t)} < f_c$, then the volumetric stress $\boldsymbol{\Sigma}^{\mathsf{vol}}$ is updated. Otherwise it is maintained to the previous value.

The first step consists in updating the values of the porosity and the average strain from the following equations.

$$\eta_{\boldsymbol{E}}^{\mathsf{vol}} = \frac{q_1 q_2 f^*(f^{(t-\delta t)}) \sinh\left(\frac{3}{2} q_2 \frac{\Sigma_{\mathsf{m}}^{\mathsf{vol}}}{\sigma_y(\bar{\varepsilon}^{(t-\delta t)})}\right)}{2\frac{\Sigma_{\mathsf{eq}}^{\mathsf{vol}}}{\sigma_y(\bar{\varepsilon}^{(t-\delta t)})}} \tag{C.2}$$

The rate δp is evaluated with the help of Table 2 where $([\dot{u}_{\mathsf{n}}],\ [\dot{u}_{\mathsf{t}}],\ [\dot{u}_{\mathsf{s}}])$ are replaced by $(h\,\delta\epsilon_{\mathsf{nn}},\ 2h\,\delta\epsilon_{\mathsf{nt}},\ 2h\,\delta\epsilon_{\mathsf{ns}})$. Then:

$$(\delta\boldsymbol{\epsilon})_{\mathsf{eq}} = \frac{2}{3}\sqrt{(\delta\epsilon_{\mathsf{nn}} - \delta p)^2 + 3(\delta\epsilon_{\mathsf{nt}})^2 + 3(\delta\epsilon_{\mathsf{ns}})^2} \quad \text{and} \quad \eta_{\delta\boldsymbol{\epsilon}} = \frac{\delta\epsilon_{\mathsf{nn}} + 2\delta p}{3\,(\delta\boldsymbol{\epsilon})_{\mathsf{eq}}} \tag{C.3}$$

$$\bar{\Sigma}_{\mathsf{nn}} = \frac{1}{q_2} H(\eta_{\delta\boldsymbol{\epsilon}}, q_1 f^*(f^{(t-\delta t)})) + \frac{4}{9} D(\eta_{\delta\boldsymbol{\epsilon}}, q_1 f^*(f^{(t-\delta t)})) \frac{\delta\epsilon_{\mathsf{nn}} - \delta p}{(\delta\boldsymbol{\epsilon})_{\mathsf{eq}}} \tag{C.4}$$

$$\bar{\Sigma}_{\mathsf{tt}} = \bar{\Sigma}_{\mathsf{ss}} = \frac{1}{q_2} H(\eta_{\delta\boldsymbol{\epsilon}}, q_1 f^*(f^{(t-\delta t)})) - \frac{2}{9} D(\eta_{\delta\boldsymbol{\epsilon}}, q_1 f^*(f^{(t-\delta t)})) \frac{\delta\epsilon_{\mathsf{nn}} - \delta p}{(\delta\boldsymbol{\epsilon})_{\mathsf{eq}}} \tag{C.5}$$

$$\bar{\Sigma}_{\mathsf{nt}} = \frac{2}{3} D(\eta_{\delta\boldsymbol{\epsilon}}, q_1 f^*(f^{(t-\delta t)})) \frac{\delta\epsilon_{\mathsf{nt}}}{(\delta\boldsymbol{\epsilon})_{\mathsf{eq}}} \tag{C.6}$$

$$\bar{\Sigma}_{\mathsf{ns}} = \frac{2}{3} D(\eta_{\delta\boldsymbol{\epsilon}}, q_1 f^*(f^{(t-\delta t)})) \frac{\delta\epsilon_{\mathsf{ns}}}{(\delta\boldsymbol{\epsilon})_{\mathsf{eq}}} \tag{C.7}$$

Then the increment of average plastic strain is computed:

$$\delta\bar{\varepsilon} = \frac{\bar{\Sigma}_{\mathsf{nn}}\,\delta\epsilon_{\mathsf{nn}} + 2\,\bar{\Sigma}_{\mathsf{nt}}\,\delta\epsilon_{\mathsf{nt}} + 2\,\bar{\Sigma}_{\mathsf{ns}}\,\delta\epsilon_{\mathsf{ns}} + \bar{\Sigma}_{\mathsf{tt}}\,\delta p + \bar{\Sigma}_{\mathsf{ss}}\,\delta p}{1 - f^{(t-\delta t)}} \tag{C.8}$$

and the porosity and plastic strain are up-dated:

$$f = f^{(t-\delta t)} + (1 - f^{(t-\delta t)})\,(\delta\epsilon_{\mathsf{nn}} + 2\,\delta p) + A(\bar{\varepsilon}^{(t-\delta t)})\,\delta\bar{\varepsilon} \quad \text{and} \quad \bar{\varepsilon} = \bar{\varepsilon}^{(t-\delta t)} + \delta\bar{\varepsilon} \tag{C.9}$$

Then, the following conditions are imposed:

$$\text{if} \quad f^{(t)} < f^{(t-\delta t)} \quad \text{then} \quad f^{(t)} = f^{(t-\delta t)}, \quad \text{and} \quad \text{if} \quad \bar{\varepsilon} < \bar{\varepsilon}^{(t-\delta t)} \quad \text{then} \quad \bar{\varepsilon}^{(t)} = \bar{\varepsilon}^{(t-\delta t)} \tag{C.10}$$

The second step consists in updating the value of the cohesive stress from the following equations. The strain p is evaluated from expressions reported in Table 2 where $([\dot{u}_{\mathsf{n}}],\ [\dot{u}_{\mathsf{t}}],\ [\dot{u}_{\mathsf{s}}])$ are replaced by $(h\,\epsilon_{\mathsf{nn}},\ 2h\,\epsilon_{\mathsf{nt}},\ 2h\,\epsilon_{\mathsf{ns}})$. Then:

$$\epsilon_{\mathsf{eq}} = \frac{2}{3}\sqrt{(\epsilon_{\mathsf{nn}} - p)^2 + 3(\epsilon_{\mathsf{nt}})^2 + 3(\epsilon_{\mathsf{ns}})^2} \quad \text{and} \quad \eta_{\boldsymbol{\epsilon}} = \frac{\epsilon_{\mathsf{nn}} + 2p}{3\,\epsilon_{\mathsf{eq}}} \tag{C.11}$$

$$\begin{cases} R_{\mathsf{n}} = \sigma_y(\bar{\varepsilon}) \left(\dfrac{1}{q_2} H(\eta_{\boldsymbol{\epsilon}}, q_1 f^*(f)) + \dfrac{4}{9} D(\eta_{\boldsymbol{\epsilon}}, q_1 f^*(f)) \dfrac{\epsilon_{\mathsf{nn}} - p}{\epsilon_{\mathsf{eq}}}\right) \\ R_{\mathsf{t}} = \sigma_y(\bar{\varepsilon}) \dfrac{2}{3} D(\eta_{\boldsymbol{\epsilon}}, q_1 f^*(f)) \dfrac{\epsilon_{\mathsf{nt}}}{\epsilon_{\mathsf{eq}}} \\ R_{\mathsf{s}} = \sigma_y(\bar{\varepsilon}) \dfrac{2}{3} D(\eta_{\boldsymbol{\epsilon}}, q_1 f^*(f)) \dfrac{\epsilon_{\mathsf{ns}}}{\epsilon_{\mathsf{eq}}} \end{cases} \tag{C.12}$$

To the end, the cohesive stress is computed:

$$\bar{\boldsymbol{R}} = \begin{cases} R_n \dfrac{[u_{\mathsf{n}}]}{[u_{\mathsf{n}}]_{\mathsf{max}}} \left(1 - \exp\left(-\alpha_{\mathsf{n}} \dfrac{[u_{\mathsf{n}}]_{\mathsf{max}}}{h}\right)\right) \\ R_t \dfrac{[u_{\mathsf{t}}]}{[u_{\mathsf{t}}]_{\mathsf{max}}} \left(1 - \exp\left(-\alpha_{\mathsf{t}} \dfrac{[u_{\mathsf{t}}]_{\mathsf{max}}}{h}\right)\right) \\ R_s \dfrac{[u_{\mathsf{s}}]}{[u_{\mathsf{s}}]_{\mathsf{max}}} \left(1 - \exp\left(-\alpha_{\mathsf{s}} \dfrac{[u_{\mathsf{s}}]_{\mathsf{max}}}{h}\right)\right) \end{cases} \tag{C.13}$$

References

[1] C. R. Tottle, Mechanical Properties of Uranium Compounds, ANL-7070 (1965).

[2] P. Chakraborty, S. B. Biner, A unified cohesive zone approach to model the ductile to brittle transition of fracture toughness in reactor pressure vessel steels, Engineering Fracture Mechanics 131 (2014) 194–209.

[3] P.-G. Vincent, Y. Monerie, P. Suquet, Porous materials with two populations of voids under internal pressure: I. Instantaneous constitutive relations, International Journal of Solids and Structures 46 (2009) 480–506.

[4] P.-G. Vincent, P. Suquet, Y. Monerie, H. Moulinec, Effective flow surface of porous materials with two populations of voids under internal pressure: I. a GTN model, International Journal of Plasticity, 56 (2014) 45–73.

[5] A. A. Benzerga, J.-B. Leblond, Ductile Fracture by Void Growth to Coalescence, Advances in Applied Mechanics 44 (2010) 169–305.

[6] A. L. Gurson, Continuum Theory of Ductile Rupture by Void Nucleation and Growth: Part I—Yield Criteria and Flow Rules for Porous Ductile Media, Journal of Engineering Materials and Technology 99 (1) (1977) 2–15.

[7] V. Tvergaard, Influence of voids on shear band instabilities under plane strain conditions, International Journal of Fracture 17 (4) (1981) 389–407.

[8] V. Tvergaard, A. Needleman, Analysis of the cup-cone fracture in a round tensile bar, Acta Metallurgica 32 (1) (1984) 157–169.

[9] J. Koplik, A. Needleman, Void growth and coalescence in porous plastic solids, International Journal of Solids and Structures 24 (8) (1988) 835–853.

[10] K.-H.Schwalbe, I. Scheider, A. Cornec, Guidelines for Applying Cohesive Models to the Damage Behaviour of Engineering Materials and Structures, Springer Science & Business Media, 2012.

[11] A. Needleman, Some issues in cohesive surface modeling, Procedia IUTAM 10 (2014) 221 – 246, mechanics for the World: Proceedings of the 23rd International Congress of Theoretical and Applied Mechanics, ICTAM2012.

[12] D. Dugdale, Yielding of steel sheets containing slits, Journal of the Mechanics and Physics of Solids 8 (2) (1960) 100 – 104.

[13] G. I. Barenblatt, The formation of equilibrium cracks during brittle fracture. General ideas and hypotheses. Axially-symmetric cracks, Journal of Applied Mathematics and Mechanics 23 (3) (1959) 622–636.

[14] A. Needleman, A Continuum Model for Void Nucleation by Inclusion Debonding, Journal of Applied Mechanics 54 (3) (1987) 525–531.

[15] A. Needleman, An analysis of tensile decohesion along an interface, Journal of the Mechanics and Physics of Solids 38 (3) (1990) 289–324.

[16] V. Tvergaard, J. W. Hutchinson, The relation between crack growth resistance and fracture process parameters in elastic-plastic solids, Journal of the Mechanics and Physics of Solids 40 (6) (1992) 1377–1397.

[17] I. Scheider, W. Brocks, Simulation of cup–cone fracture using the cohesive model, Engineering Fracture Mechanics 70 (14) (2003) 1943–1961.

[18] J.-L. Chaboche, F. Feyel, Y. Monerie, Interface debonding model: a viscous regularization with a limited rate dependency, International Journal of Solids and Structures 38 (18) (2001) 3127–3160.

[19] T. Siegmund, A. Needleman, A numerical study of dynamic crack growth in elastic-viscoplastic solids, International Journal of Solids and Structures 34 (7) (1997) 769–787.

[20] K. L. Nielsen, J. W. Hutchinson, Cohesive traction-separation laws for tearing of ductile metal plates, International Journal of Impact Engineering 48 (2012) 15–23.

[21] P. B. Woelke, M. D. Shields, J. W. Hutchinson, Cohesive zone modeling and calibration for mode I tearing of large ductile plates, Engineering Fracture Mechanics 147 (2015) 293–305.

[22] R. G. Andersen, P. B. Woelke, K. L. Nielsen, Cohesive traction-separation relations for plate tearing under mixed mode loading, European Journal of Mechanics / A Solids 71 (2018) 199–209.

[23] R. G. Andersen, C. L. Felter, K. L. Nielsen, Micro-mechanics based cohesive zone modeling of full scale ductile plate tearing: From initiation to steady-state, International Journal of Solids and Structures 160 (2019) 265–275.

[24] Y. Bao, T. Wierzbicki, On fracture locus in the equivalent strain and stress triaxiality space, International Journal of Mechanical Sciences 46 (1) (2004) 81–98.

[25] A. A. Benzerga, J.-B. Leblond, A. Needleman, V. Tvergaard, Ductile failure modeling, International Journal of Fracture 201 (1) (2016) 29–80.

[26] V. Tvergaard, J. W. Hutchinson, Effect of strain-dependent cohesive zone model on predictions of crack growth resistance, International Journal of Solids and Structures 33 (20) (1996) 3297–3308.

[27] V. Tvergaard, Relations between Crack Growth Resistance and Fracture Process Parameters Under Large Scale Yielding, in: IUTAM Symposium on Nonlinear Analysis of Fracture, Solid Mechanics and its Applications, Springer, Dordrecht, 1997, pp. 93–104.

[28] A. Banerjee, R. Manivasagam, Triaxiality dependent cohesive zone model, Engineering Fracture Mechanics 76 (12) (2009) 1761–1770.

[29] M. Rajendran, I. Scheider, A. Banerjee, Stress State Dependent Cohesive Zone Model for Thin Walled Structures, Key Engineering Materials 417-418 (2010) 353–356.

[30] I. Scheider, Derivation of separation laws for cohesive models in the course of ductile fracture, Engineering Fracture Mechanics 76 (10) (2009) 1450–1459.

[31] T. Siegmund, W. Brocks, Prediction of the Work of Separation and Implications to Modeling, International Journal of Fracture 99 (1-2) (1999) 97–116.

[32] T. Siegmund, W. Brocks, A numerical study on the correlation between the work of separation and the dissipation rate in ductile fracture, Engineering Fracture Mechanics 67 (2) (2000) 139–154.
[33] M. Anvari, I. Scheider, C. Thaulow, Simulation of dynamic ductile crack growth using strain-rate and triaxiality-dependent cohesive elements, Engineering Fracture Mechanics 73 (15) (2006) 2210–2228.
[34] M. Anvari, J. Liu, C. Thaulow, Dynamic ductile fracture in aluminum round bars: experiments and simulations, International Journal of Fracture 143 (4) (2007) 317–332.
[35] M. Gărăjeu, P. Suquet, Effective properties of porous ideally plastic or viscoplastic materials containing rigid particles, Journal of the Mechanics and Physics of Solids 45 (6) (1997) 873–902.
[36] C. C. Chu, A. Needleman, Void Nucleation Effects in Biaxially Stretched Sheets, Journal of Engineering Materials and Technology 102 (3) (1980) 249–256.
[37] J.-C. Michel, P. Suquet, F. Thébaud, Une modélisation du rôle des interfaces dans le comportement des composites à matrice métallique, Revue Européenne des Éléments Finis 3 (4) (1994) 573–595.
[38] Y. Monerie, V. Acary, Formulation dynamique d'un modèle de zone cohésive tridimensionnel couplant endommagement et frottement, Revue Européenne des Eléments Finis 10 (02-03-04) (2001) 489–503.
[39] P. M. Suquet, Discontinuities and Plasticity, in: Nonsmooth Mechanics and Applications, International Centre for Mechanical Sciences, Springer, Vienna (1988) 279–340.
[40] J. Oliver, M. Cervera, O. Manzoli, Strong discontinuities and continuum plasticity models: the strong discontinuity approach, International Journal of Plasticity 15 (3) (1999) 319–351.
[41] F. M. Rashid, A. Banerjee, Implementation and validation of a triaxiality dependent cohesive model: experiments and simulations, International Journal of Fracture 181 (2) (2013) 227–239.
[42] F.M. Rashid, A. Banerjee, Simulation of fracture in a low ductility aluminum alloy using a triaxiality dependent cohesive model, Engineering Fracture Mechanics 179 (C) (2017) 1–12.
[43] J. J. C. Remmers, R. de Borst, C. V. Verhoosel, A. Needleman, The cohesive band model: a cohesive surface formulation with stress triaxiality, International Journal of Fracture 181 (2) (2013) 177–188.
[44] N. Aravas, On the Numerical Integration of a Class of Pressure-Dependent Plasticity Models, International Journal for Numerical Methods in Engineering 24 (1987) 1395–1416.
[45] M. Jean, V. Acary, Y. Monerie, Non-smooth contact dynamics approach of cohesive materials, Philosophical Transactions of the Royal Society A: Mathematical, Physical and Engineering Sciences 359 (1789) (2001) 2497–2518.
[46] J. C. Michel, H. Moulinec, P. Suquet, Effective properties of composite materials with periodic microstructure: a computational approach, Computer Methods in Applied Mechanics and Engineering 172 (1) (1999) 109–143.
[47] F. Perales, S. Bourgeois, A. Chrysochoos, Y. Monerie, Two field multibody method for periodic homogenization in fracture mechanics of nonlinear heterogeneous materials, Engineering Fracture Mechanics 75 (11) (2008) 3378 – 3398, local Approach to Fracture (1986–2006): Selected papers from the 9th European Mechanics of Materials Conference.
[48] F. Perales, F. Dubois, Y. Monerie, B. Piar, L. Stainier, A NonSmooth Contact Dynamics-based multi-domain solver, European Journal of Computational Mechanics 19 (4) (2010) 389–417.
[49] V. Acary, Y. Monerie, Nonsmooth fracture dynamics using a cohesive zone approach, Research Report, INRIA (2006).
[50] M. Jean, The non-smooth contact dynamics method, Computer Methods in Applied Mechanics and Engineering 177 (3) (1999) 235–257.
[51] M. Ortiz, A. Pandolfi, Finite-deformation irreversible cohesive elements for three-dimensional crack-propagation analysis, International Journal for Numerical Methods in Engineering 44 (9) (1999) 1267–1282.
[52] W. Brocks, A. Eberle, S. Fricke, H. Veith, Large stable crack growth in fracture mechanics specimens, Nuclear Engineering and Design 151 (2) (1994) 387–400.
[53] T. Siegmund, W. Brocks, The Role of Cohesive Strength and Separation Energy for Modeling of Ductile Fracture, in Fatigue and Fracture Mechanics: 30th Volume, ed. K. Jerina and P. Paris, West Conshohocken, PA: ASTM International (2000), 139–151.
[54] F. Perales, Fissuration des matériaux à gradient de propriétés : application au Zircaloy hydruré, Ph.D. thesis, Montpellier 2 (2005).
[55] W. Brocks, D. Klingbeil, G. Künecke, D.-Z. Sun, Application of the Gurson Model to Ductile Tearing Resistance, in Constraint Effects in Fracture Theory and Applications: Second Volume, ed. M. Kirk and A. Bakker, West Conshohocken, PA: ASTM International (1995), 232–252.
[56] ASTM, ASTM e1820-18, standard test method for measurement of fracture toughness, Standard, ASTM International, West Conshohocken, PA (Jan. 2018).
[57] X.-K. Zhu, J. A.Joyce, Review of fracture toughness (G, K, J, CTOD, CTOA) testing and standardization, Engineering Fracture Mechanics 85 (2012) 1–46.
[58] J. Besson, Continuum models of ductile fracture: A review, International Journal of Damage Mechanics 19 (2010) 3–52.
[59] N. Blal, L. Daridon, Y. Monerie, S. Pagano, Artificial compliance inherent to the intrinsic cohesive zone models: Criteria and application to planar meshes, International Journal of Fracture 178 (1-2) (2012) 71–83.
[60] V. Tomar, J. Zhai, M. Zhou, Bounds for element size in a variable stiffness cohesive finite element model, International Journal for Numerical Methods in Engineering 61 (11) (2004) 1894–1920.
[61] H. D. Espinosa, P. D. Zavattieri, A grain level model for the study of failure initiation and evolution in polycrystalline brittle materials. Part I: Theory and numerical implementation, Mechanics of Materials 35 (3) (2003) 333–364.